2013

CHARACTERIZATION OF AND CONTROLLING MORPHOLOGY OF ULTRA-THIN NANOCOMPOSITES

Guy C. Laine
University of Kentucky, guyclaine@gmail.com

STUDENT AGREEMENT:

I represent that my thesis or dissertation and abstract are my original work. Proper attribution has been given to all outside sources. I understand that I am solely responsible for obtaining any needed copyright permissions. I have obtained and attached hereto needed written permission statements(s) from the owner(s) of each third-party copyrighted matter to be included in my work, allowing electronic distribution (if such use is not permitted by the fair use doctrine).

I hereby grant to The University of Kentucky and its agents the non-exclusive license to archive and make accessible my work in whole or in part in all forms of media, now or hereafter known. I agree that the document mentioned above may be made available immediately for worldwide access unless a preapproved embargo applies.

I retain all other ownership rights to the copyright of my work. I also retain the right to use in future works (such as articles or books) all or part of my work. I understand that I am free to register the copyright to my work.

REVIEW, APPROVAL AND ACCEPTANCE

The document mentioned above has been reviewed and accepted by the student's advisor, on behalf of the advisory committee, and by the Director of Graduate Studies (DGS), on behalf of the program; we verify that this is the final, approved version of the student's dissertation including all changes required by the advisory committee. The undersigned agree to abide by the statements above.

Guy C. Laine, Student

Dr. Eric A. Grulke, Major Professor

Dr. Tom Dziubla, Director of Graduate Studies

CHARACTERIZATION OF AND CONTROLLING MORPHOLOGY OF ULTRA-THIN NANOCOMPOSITES

THESIS

A thesis submitted in partial fulfillment of the
requirements for the degree of Master of Science in
Chemical Engineering in the College of Engineering
at the University of Kentucky

By

Guy Christopher Laine

Lexington, Kentucky

Director: Dr. Eric A. Grulke, Professor of Chemical Engineering

Lexington, Kentucky

2013

ABSTRACT OF THESIS

CHARACTERIZATION OF AND CONTROLLING MORPHOLOGY OF ULTRA-THIN NANOCOMPOSITES

Ultrathin film nanocomposites are becoming increasingly important for specialized performance of commercial coatings. Critical challenges for ultrathin film nanocomposites include their synthesis and characterization as well as their performance properties, including surface roughness, optical properties (haze, refractive index as examples), and mechanical properties. The objective of this work is to control the surface roughness of ultrathin film nanocomposites by changing the average particle size and the particle volume fraction (loading) of monomodal particle size distributions. This work evaluated one-layer and two-layer films for their surface properties. Monodispersed colloidal silica nanoparticles were incorporated into an acrylate-based monomer system as the model system. Ultrathin nanocomposites were prepared with three different size colloidal silica (13, 45, and 120 nm nominal diameters) at three different particle loadings (20, 40, and 50 vol. % inorganic solids). Silica particles were characterized using DLS and TEM. AFM was used to measure the root mean square roughness (R_q), ΔZ, and location-to-location uniformity of one-layer and two-layer nanocomposite coatings. Developing an understanding about the properties affected by the type and amount of particles used in a nanocomposite can be used as a tool with nanocharacterization techniques to quickly modify and synthesize desired ultrathin film coatings.

KEYWORDS: Ultrathin film nanocomposite, Surface Morphology, Spin Coating, Particle Loading, Particle Size

Guy Christopher Laine

November 20th, 2013

CHARACTERIZATION OF AND CONTROLLING MORPHOLOGY OF ULTRA-THIN NANOCOMPOSITES

By

Guy Christopher Laine

Dr. Eric A. Grulke

Director of Thesis

Dr. Tom Dziubla

Director of Graduate Studies

November 20th, 2013

(TO MY PARENTS)

Acknowledgement

First, I would like to express my thanks to the members of my thesis committee, Dr. Eric A. Grulke, Dr. Stephen E. Rankin, and Dr. Thomas John Balk for taking the time to review my work. I would especially like to thank my advisor, Dr. Eric A. Grulke, for guiding me to be an independent researcher and providing the opportunity to work on projects related to chemistry, materials and polymer science. I would also like to think my lab mates (Dr. Peng Wu, Dr. Courtney Harrison, Dr. Vinod Kanniah, Binghui Wang, Natalia Mandzy, Joseph Alexander) and student researcher Nathan McKee for their help and support in my research work at the University of Kentucky.

Table of Contents

List of Tables

List of Figures

Chapter 1

Chapter 2

Chapter 3

Chapter 4

Chapter 1 Introduction

Nanoparticles are defined as any particle having a dimension between 1 nm and 100 nm [2]. There is wide interest for uses of inorganic/organic nanoparticles in biomedical, pharmaceutical, optical, and electrical applications. The addition of nanoparticles to a continuous polymer matrix is defined as a nanocomposite. Nanoparticles previously incorporated into polymer matrices include metals, metal oxides, metal nitrides, and metal carbides [3, 4]. Combining inorganic nanoparticles and polymer matrices allows for the development of a wide variety of nanocomposite materials that combine the physical properties of the respective constituents. Systems can have single or multiple phases of nanoparticles/polymer components. Systems that incorporate more than one type of polymer, in which chain segments of the two polymers are dispersed through one another, are called interpenetrating polymer networks. Selecting appropriate combinations of physical properties for each species in a nanocomposite allow researchers to produce nanocomposites with wide ranges of performance properties.

Nanocomposite coatings are used in a wide variety of optical and electrical applications from eyeglass lenses to optical filters for the visible, infrared, and ultraviolet regions of light. Ultra-thin film nanocomposites are coatings that have a thickness less than 500 nm and are typically less than 200 nm [5]. Ultra-thin nanocomposite coatings have a wide range of applications ranging from optical, magnetic, electrical, and photonic systems [6-8]. Ultra-thin film nanocomposite coatings are primarily used as filters for various ranges of light whether visible, infrared, or ultraviolet light. Polymer-nanoparticle nanocomposite coatings are extremely important in a wide variety of applications including glasses to jet canopies. Table 1.1 shows examples of attributes of interpenetrating polymer networks (IPN) and nanoparticle composite (NC) technologies. Interpenetrating polymer networks can be included in a nanocomposite system.

Table 1.1 Performance properties of interpenetrating polymer networks (IPN) and nanoparticle composite (NC) technologies.

Property/performance	Example system	Technology	References
Mechanical			
Creep resistance improvement	Silica nanoparticles functionalized with silanes, in polypropylene	Semi-IPN; NC	[9], [10]
Increasing tensile strength and notched impact strength at low NP loadings	Silicapolypropylene nanocomposites (in-situ crosslinking)	Semi-IPN; NC	[11]
Increase in elastic modulus and hardness while retaining transparency	Nanosilica in urethane dimethacrylate + bisphenol-A diglycidyl ether epoxy	IPN, NC	[12]
Chemical resistance, anti-adhesion	Metal oxide nanoparticles in poly(disiloxane)	NC	[13]
Improved mechanical damping; potential for improved impact	BaTiO3 in polyurethane/unsaturated polyester resin	IPN	[14]
Reduced crazing, increased toughness	Polycarbonate and poly(methyl methacrylate)	IPN	[15]
Increased modulus and hardness	Zinc oxide nanoparticles in polycarbonate	NC	[16]
Electrical/optical			
Conduction mechanism w/semiconducting nanoparticles and conducting IPNs	Varied (review article)	NC, IPNs	[17]
Charge transfer in photovoltaics	Conjugated conducting polymers, titania nanoparticles	NC, IPNs	[18]
High energy density capacitors	Barium titanate nanoparticles in polycarbonate	NC	[19]
Nanocomposite foils for solar glazing, attenuation of heat gain and UV	Polycarbonate, poly(vinyl butyral), metal oxide nanoparticles	NC	[20]
Semi-interpenetrating polymer network for conducting applications	Poly(ethylene oxide) with poly(3,4-ethylenedioxythiophene) (PEDOT)	IPN	[21]
Nonlinear optical properties	Polycarbonate-polyurethane-polymethacrylate	IPN	[8, 22]

1.1 Nanoparticles for Ultrathin Nanocomposites

Polymer-nanocomposites have a wide range of properties, which can be controlled to tailor ultra-thin films to specific specifications. Some of the critical properties of these coatings include:

- Mechanical properties, including modulus, scratch, and hardness.
- Adhesion properties - interlaminar adhesion from layer to layer, and adhesion of nanocomposites to substrate versus temperature, and solvent exposure.
- Optical properties, including clarity, haze, and refractive index.
- Flex - particularly on soft polymer substrates.
- Rapid polymerization rates - 90% conversion or tacky, minutes to full cure.

Control of these properties requires control of the polymer chemistry, orientation of the nanoparticles, nanoparticle packing and size, particularly in reference to the layer thickness. Optical and mechanical properties of polymer coatings can be affected by a number of factors including but not limited to: inter-laminar adhesion of nanocomposite layers, viscosity of the fluids, particle loading, rate of coating speed, and surface tension. Figure 1.1 shows the process flow diagram for producing ultrathin nanocomposites with a monomer-solvent-nanoparticle solution. Nanoparticles become trapped in the polymer matrix after they are spin coated onto a substrate, forming a nanocomposite.

Few studies have been performed that analyze the surface morphology of ultra-thin nanocomposites based on concentration and particle size of the nanoparticles incorporated into the nanocomposite. Previous studies report using bimodal mixtures of silica nanoparticles (10 nm and 100 nm nominal diameters) in an acrylate-based monomer system for study [1]. Kanniah reported no change in the surface roughness as the weight fraction of 100 nm size particles increased from 0.1 to 0.35 for bimodal nanocomposites. However, no data was present regarding the effect of the concentration of unimodal particle size mixtures on the surface roughness of ultrathin films. To better understand the behavior of bimodal nanocomposites it is necessary to first understand the behavior of unimodal nanocomposites.

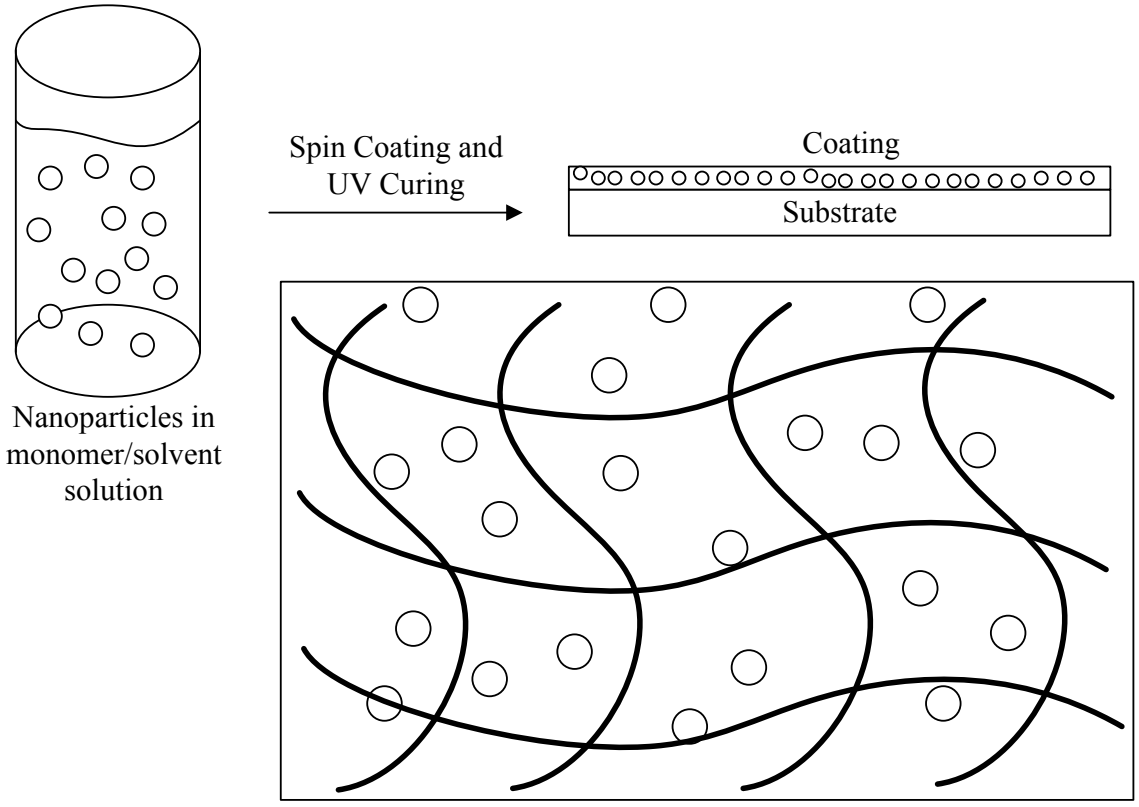

Figure 1.1 Process flow diagram for producing ultra-thin nanocomposites with a monomer-solvent-nanoparticle solution. Nanoparticles become trapped in the polymer matrix.

The main objective of this work was to determine the effect of particle size and particle loading on the surface morphology of ultrathin film optical coatings. The technology used to fabricate these films was a nanoparticle-acrylate monomer nanocomposite system, with spin coating deposition methods, to achieve ultrathin nanocomposite films. The effect of nanoparticle loading and nanoparticle size on surface morphology of ultrathin film acrylate-based nanocomposites will be investigated. Researchers do not fully understand the affect these properties have on the surface roughness. Dynamic light scattering and transmission electron microscopy will be used to characterize and understand the particles used in the nanocomposite. Atomic force microscopy will be used to determine the surface roughness of the nanocomposite films. Through these methods a better understanding of the particle loading and particle size on the surface roughness of ultrathin film nanocomposites will be obtained.

1.2 Nanoparticle Characterization

Nanoparticles come in a wide variety of sizes and shapes, and therefore, careful characterization is needed to truly understand the properties of the nanoparticles and their behavior in different systems. Moreover, surface properties such as area, energy, porosity, and functionalization can affect how nanoparticles behave in solution or in a solid phase [4, 23]. Nanoparticles can be characterized using a wide array of techniques including, but not limited to, transmission electron microscopy (TEM), scanning electron microscopy (SEM), atomic force microscopy (AFM), dynamic light scattering (DLS), size exclusion chromatography (SEC), small angle neutron scattering (SANS), matrix-assisted laser desorption/ionization time-of-flight mass spectrometry (MALDI-TOF), and electrospray differential mobility analysis (ES-DMA) [24].

For purposes of this document we will focus on TEM, DLS, and AFM. TEM and DLS will be used to obtain the particle size distribution, providing information about the agglomeration/aggregation of the nanoparticles. Agglomeration is the grouping of particles based upon affinity for one another, and typically occurs in liquid solutions with charge instability. Aggregation takes place when the particles are ‘fused’ together and result in larger solids in solution or more commonly in the form of powder. Uniform, stable, and monodispersed nanoparticles of less than 150 nm in liquid dispersion are

critical for synthesizing ultra-thin nanocomposite coatings. Dispersing particles into solution can be very difficult as shown by Mandzy, *et. al.*[25]. Therefore, it is important to have particles which were formulated in dispersion. Figure 1.2 shows the difference between monodispersed, agglomerated, and aggregated particles. AFM will be used to analyze the surface morphology of the nanocomposites.

The main objectives are: to better understand the characterization techniques needed to appropriately classify nanoparticle size distributions, and control the surface morphology of ultrathin nanocomposites by varying the nanoparticle filler mixtures used to produce the material. Particle size distributions are typically performed using TEM/SEM for solids and DLS for liquid dispersions. Information gained from these measurements provides valuable information about the nanoparticles used in a system. Measuring nanoparticles using more than one method provides a reliable way to validate results.

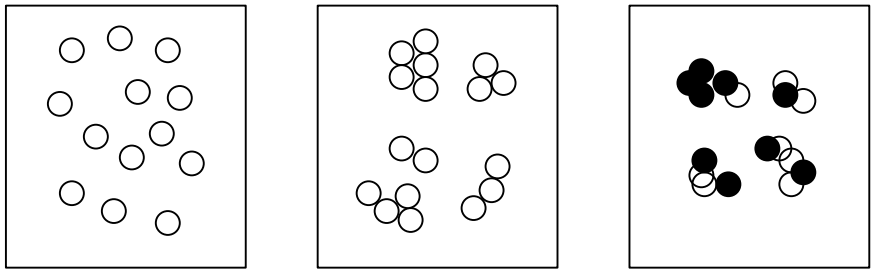

Figure 1.2 Sketch of monodispersed, agglomerated particles in solution, and aggregated particles are fused as a solid (either in powder form or in dispersion).

1.3 Nanocomposite Coating Morphology

Nanosized fillers can enhance the physical properties of polymers but often do not have adverse effects on polymer processing [26, 27]. Having precise control of nanoparticle dispersion in precursor solutions and polymeric matrices is essential to developing high-performance nanocomposites [28]. This is due to interactions between nanoparticles. The systems used in this study are based on acrylate monomers providing the necessary flexible continuous phase, which also helps promote homogeneous nanoparticle dispersion when nanofillers are added [29]. One of the most important aspects of nanocomposites is the interfacial interactions between polymer and nanoscale filler [29]. The overall size and surface properties will ultimately govern the properties of the interactions between polymer and nanoparticle.

The main objective of this work is to control the surface morphology of ultrathin nanocomposites by varying the nanoparticle filler mixtures used to produce the material. Understanding the morphology of such nanocomposites provides researchers with an understanding of how to make highly specific types of nanocomposites. For example, optical coating materials often have multiple layers of nanocomposites with the same polymer base. Within each layer are nanoparticles with varying refractive indices. The change in refractive indices between the layers can be optimized for a desired reflection or transmittance of light for a given range of wavelengths [30]. Generally, tolerances must be less than +/- 5nm for proper control of optical properties. Therefore, it is imperative to have exact control of the surface roughness of each nanocomposite layer.

1.4 Thesis Overview

The objective of this thesis is to provide an understanding of how the particle size and concentration govern the surface morphology of ultra-thin film nanocomposites. Low particle concentrations of precursor solutions can still provide a relatively high loading of particles in a nanocomposite. Details on experimental methods are found within each chapter as needed.

This chapter summarizes and outlines the relevance and objectives contained in this dissertation. Chapter 2 addresses nanoparticle characterization and morphology. Chapter 3 explains the experimental methods used to synthesize ultra-thin film nanocomposites. Chapter 4 explains the effect particle size and particle concentration have on the surface morphology of ultra-thin nanocomposite films. Chapter 5 summarizes the results found in Chapters 2-4.

George H. Heilmeir is a well-known engineer and businessman who developed a set of questions for new research projects or new product development, known as the Heilmeier's catechism [31]:

- What are you trying to do?
- How is it done today?
- What is new in your approach?
- Who cares?
- What difference will a successful project make?
- What are the risks / payoffs?

Providing answers to Heilmeier' catechism helps create a basis for the research project, improves project planning, and possible milestones. Table 1.2 answers Heilmeier's questionnaire for developing low haze ultrathin film nanocomposites for optical applications. Furthermore, advancing technologies that could lead to new markets are, but not limited to:

- Gradients of refractive index through the layer or near the layer interface
- Improved impact resistance and interfacial adhesion

Table 1.2 Heilmeier's questionnaire: Developing low haze ultrathin film nanocomposites.

What are you trying to do?	Control surface roughness/morphology for low haze ultrathin nanocomposite films for optical product applications. Applications include but not limited to hydrophobic and antireflective coatings.
How is it done today?	It is done today by nanoparticle-acrylate monomer nanocomposite system with various monodispersed nanoparticles of different refractive indices.
What's new in your approach?	• Vary the concentration of nanofillers to control surface roughness for improved control of surface roughness. May lead to: • Simple tool/method to control the surface morphology • Changing the particle size of the nanofiller to control the surface roughness.
Who cares?	• Optical coating suppliers who develop optical products with desired specifications. Other specialty coatings manufacturers (Circuit /Photoresist manufactures). • Researchers with areas of interest such as optical coatings, reactive surface coatings (self-cleaning), protective-fuel cell membranes; interlayer adhesion aids, laminated nanocomposites.
What difference will a successful project make?	• Understanding surface morphology can allow manufactures or researchers develop very specialized coatings with better control. Optical property interdependence would help develop different specialty coating product applications. • Reducing multiple layers for antireflective coatings would reduce the manufacturing cost and eventually product price. • Low-cost option for control of surface morphology
What are the risks/payoffs?	• Increasing surface roughness for hydrophobicity without compromising transparency (low haze) in an ultrathin film. • Characterizing nanoparticle segregation for ultrathin film coatings is always required. • Time loss to obtain information about a single coating recipe.
What are the milestones to check for success?	• Check surface roughness variances between concentration and particle size. • Study the consistency of the surface properties of polymer nanocomposites with a silica-acrylate model system.

- Adhesion to other polymers, oleophilic surfaces and metals
- Transfer to new matrix polymers: polyethylene terephthalate (PET) for flexible, printable decals; polycarbonate (PC) for high impact and ballistic applications (clear optical coatings on PC for military applications)
- Improved scratch and impact resistance

The importance of ultra-thin film nanocomposites is growing as technology is becoming smaller and smaller. Being able to control not only the surface roughness but other properties, type of particle, the polymer base, thickness, etc. of ultra-thin coatings can lead to diverse applications.

Chapter 2 Nanoparticle Characterization

2.1 Introduction

Nanoparticles, nanoparticle additives, and engineered nanomaterials (ENMs) have become an ever-increasing field of study in the last decade. Many companies have been producing various types of engineered nanoparticles for applications ranging from biomedical and food applications to painting and optically transparent coatings. However, many companies have a hard time maintaining precise control over the particle size distributions of product in a single batch and from batch to batch. Hence, it is imperative for researchers to characterize nanoparticles obtained from suppliers and synthesized in-house. This becomes vital when trying to incorporate nanoparticles into ultra-thin film nanocomposites with thicknesses of a few nanometers or less.

Three different commercial silica nanoparticle sizes were measured: IPA-ST (10-15), IPA-ST-L (40-50), and IPA-ST-ZL (70-100).Note: for IPA-ST-ZL Elongated particles have a diameter of 9-15 nm with a length of 40-100 nm. Silica particles were chosen due to their wide use in coating applications. Furthermore, it was important to have particles which would be smaller than the ultrathin polymer film thickness to ensure encapsulation of the particles in the ultrathin nanocomposites. Particle size was determined using a 90 Plus dynamic light scattering (DLS) analyzer from Brookhaven Instrument, USA; and electron microscopy using a JEOL 2010F Transmission Electron Microscopy, Japan. The DLS provides researchers with the hydrodynamic radius of a particle while TEM will provide the primary particle size.

2.2 Experimental

ORGANOSILICASOL™ is colloidal silica (not aggregated); monomodel dispersions in isopropanol (IPA) produced by Nissan Chemical. ORGANOSILICASOL™ is used for a wide range of coating materials to help improve the scratch, chip, and mar resistance for: hard-coating agents for plastics, nanocomposites, UV/EB curable coatings, paint modification, micro-filler for film, nanofiller, heat resistance, weather resistance, and other applications [32]. The colloidal solution can come in a variety of particle sizes with a variety of organic solvents. For the system of interest, isopropanol alcohol is the organic solvent of choice. Nissan Chemical

also promotes the dispersability, stability, and narrow particle size distributions of ORGANOSILICASOL™. Table 2.1 shows the manufacturer's properties of three different types of ORGANOSILICASOL™ colloidal solutions that were measured and used to make ultra-thin film nanocomposites. DLS and TEM will be used to verify the particle size of dilute colloidal silica solutions of the three samples.

Table 2.1 ORGANOSILICASOL™ colloidal silica manufacturer properties reported from Nissan Chemical America Corporation. *Elongated particles have a diameter of 9-15 nm with a length of 40-100 nm [32].

ORGANOSILICASOL ™ colloidal silica					
Type	Size [nm]	SiO_2 [wt %]	μ [mPa.s.]	S.G.	Solvent
IPA-ST	10 - 15	30-31	< 15	0.96-1.02	Isopropanol
IPA-ST-L	40 - 50	30-31	< 15	0.96-1.02	Isopropanol
IPA-ST-ZL	70-100*	30-31	< 15	0.96-1.02	Isopropanol

The three different samples of colloidal silica were used to incorporate into nanocomposite precursor solutions. Precursor solutions for spin coating contained less than 10 wt% silica. Concentrated samples provided by the manufacturer are difficult to measure due to the high concentration of silica and turbidity. All samples used to measure the particle size were diluted to less than 1 wt% dispersions in IPA.

2.3 Dynamic Light Scattering (DLS)

One of the most widely used methods to measure the particle size of sub-micron particles (less than 1 um) and nanoparticles is dynamic light scattering (DLS). This is also known as photon correlation spectroscopy or quasi-elastic light scattering [33]. DLS utilizes the diffusivity of small particles experiencing Brownian motion in solution to determine the particle size (hydrodynamic diameter) [34]. Light scattered by particles in solution causes fluctuations in the measured intensity of light by a detector. Particles which undergo Brownian motion in solution can be described by the autocorrelation function which decays exponentially with time. Equation 2.1 is the autocorrelation function which determines how long a given measured signal stays the same. Equation 2.2 is obtained by using the Siegert relationship (assuming scattering is homodyne and a random Gaussian process), as well as, approximating Equation 2.1 since infinite time limits cannot be achieved [35]. Equation 2.2 relates intensity to the electric field autocorrelation function. The electric field autocorrelation function, *g(t)*, represented in Equation 2.2 is generally normalized and represented by an exponential decay as shown by Equation 2.3.

$$G(\tau) = \lim_{T\to\infty} \frac{1}{2T}\int_{-T}^{T} I(t)I(t+\tau)dt = < I(t)I(t+\tau) > \quad \text{Equation 2.1}$$

$$G(\tau) = B\,(1 + f|g(t)|^2) \quad \text{Equation 2.2}$$

$$g(t) = e^{-\Gamma t} \quad \text{Equation 2.3}$$

$$\Gamma = -Dq^2 \quad \text{Equation 2.4}$$

For translational diffusion, Γ, the decay rate is represented is shown in Equation 2.4. Furthermore, the scattering vector, q, and translational diffusion coefficient, D, are represented by Equation 2.5 and Equation 2.6, respectively. Equation 2.6 is the Stokes-Eienstein equation which is used to calculate the size of the particles in solution. The interactions between particles and fluid are then measured relating to intensity.

$$q = \frac{4\pi n}{\lambda} \sin\left(\frac{\theta}{2}\right) \qquad \text{Equation 2.5}$$

$$D = \frac{k_B T}{6\pi\eta R_h} \qquad \text{Equation 2.6}$$

The translational diffusion coefficient describes motion, size, shape, and surface of the particles in motion [36]. Factors that influence the diffusion of particles through a fluid media include but are not limited to: ionic strength, surface chemistry, irregular shaped particles, and temperature. Figure 2.1 shows by example the hydrodynamic radius of a particle in solution. The hydrodynamic radius includes the core of the particle, additional layers/ligands or particles adsorbed on the surface of the particles, and the solvation layer made up of counter-ions. Possible small chain groups, such as a carboxyl group, could be present on the surface.

When measuring particles using dynamic light scattering it is important to have dilute solutions or suspensions. Because we measure the scattering of light due to the movement of particles in their surrounding media, concentrated solutions can cause discrepancies in the measurements. Turbid dispersions or dispersions consisting of high concentrations of particles typically result in either no transmission of light through the sample cell or cause multiple scattering of light waves. This directly affects the determination of the particle size by either providing no measurement or an incorrect estimate of the particle size [36]. Final diluted dispersions of particles measured using DLS were approximately 0.1 wt% of silica in IPA.

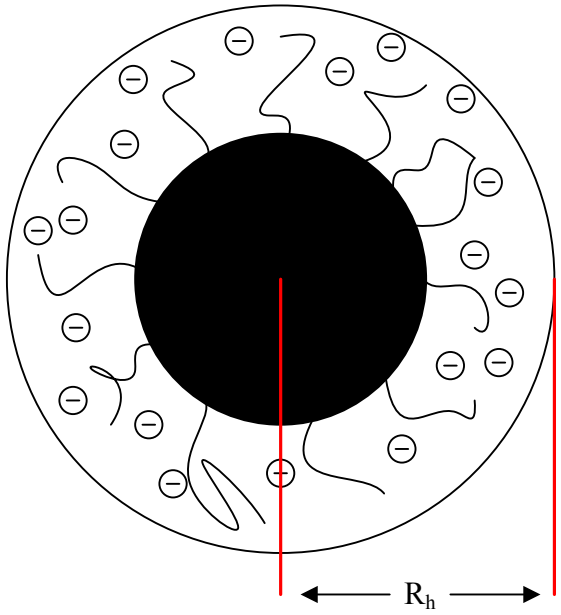

Figure 2.1 An example of the spatial region included in the hydrodynamic radius of a particle calculated using dynamic light scattering techniques. The radius consists of any physical or electrical layers surrounding the particle.

2.3.1 Dynamic Light Scattering - Results

Solutions of the three different particle sizes (IPA-ST, IPA-ST-L, IPA-ST-ZL) were measured on the 90Plus Particle Size Analyzer. Using the BIC Particle Solutions software version 1.1, the intensity-weighted, number-weighted, and volume-weighted distributions can be obtained when measuring the particle size. These distributions are derived via CONTIN (*CON*strained regularization method for *IN*verting data), a non-linear regularization method developed by S. Provencher, which looks for the "*simplest solution consistent with prior knowledge and experimental data" [37, 38]*. The correlation function is then transformed using the CONTIN algorithm to obtain the intensity-weighted distribution function. From the intensity-weighted distribution function, number-weighted and volume-weighted distributions are obtained. For purposes of this section, the volume distributions will be used to compare the particle size to TEM in the next section. The intensity-weighted and number-weighted distributions for each corresponding volume-weighted distribution can be found in Appendix A.

The volume-weighted size distribution is related to the intensity-weighted distribution by Equation 2.7. Moreover, the number based size distribution is related to the intensity weighted and volume weighted distributions by Equation 2.8. Where, M, is the Mie light scattering coefficient (M = 1 for particles whose diameter is less than 25 nm). The volume-weighted particle size distribution best represents the volume or mass of particles which are in dispersion. The number-weighted distributions represent how many particles of each size are present in dispersion.

$$G_V(d) = \frac{G_I(d)}{d^3} = \frac{G_I(d)}{8r^3M} \qquad \text{Equation 2.7}$$

$$G_N(d) = \frac{G_V(d)}{d^3} = \frac{G_I(d)}{64r^6M} \qquad \text{Equation 2.8}$$

All samples were measured at 25°C for 300 seconds with an equilibrium time of 30 seconds between each run. The dust cutoff was set at 30.00. The dust cutoff is an algorithm built within the program used to help reject data corrupted by light scattering caused by dust. For smaller particles (less than 30 nm), the dust cutoff should be

lowered. All data sets observed a 98% or greater data retention rate, which proved an appropriate dust cutoff level was used.

Figures 2.2 and 2.3 show the volume and intensity weighted differential and cumulative frequency distribution functions for IPA-ST colloidal suspension of silica nanoparticles. Similarly, Figures 2.4, 2.5, and 2.6 show the volume, intensity, and number-weighted differential and cumulative frequency distribution functions for IPA-ST-L. Figure 2.7 shows the volume-weighted differential and cumulative particle sized distribution for and IPA-ST-ZL colloidal silica dispersion suspension of silica nanoparticles. All concentrations in the dispersions were less than 0.1 wt% silica.

Figure 2.2 shows the averaged volume-based particle size distribution of an IPA-ST dispersion in isopropanol. The volume-based distribution is slightly log normally distributed with an average particle size of 5 nm. The averaged intensity-based particle size distribution of IPA-ST is found in Figure 2.3. The particle size distribution of the intensity-based distribution is bimodal largely due to agglomeration of smaller particles in solution. The bimodal distributions also appear to be more normally distributed. The larger distribution average has an average approximately eight times larger than the smaller particle size distribution. The number-based distribution can be found in Appendix A and shows good agreement with the volume-weighted distribution.

Figure 2.4 shows the averaged volume-based particle size distribution of an IPA-ST-L dispersion. The distribution is slightly log normally distributed with a slight skew towards larger particles. Some agglomeration is present in the sample as shown by the smaller larger distributions at 113 nm and 162 nm. Further comparison with the intensity-weighted particle size distribution found in Figure 2.5 shows that the IPA-ST colloidal solution is bimodal and not normally or log normally distributed. The intensity of the larger particle size distribution suggests a large amount of agglomeration in the sample. The average particle size of IPA-ST-L particles was approximately 35 nm. Particle sizes ranged between 25 nm and 55 nm. The number-based particle size distribution most clearly represents the size of the particles and is log normally distributed in Figure 2.6 with an average particle size of 36 nm. Further analysis of the particles via TEM was needed to determine the correct particle size distribution for IPA-ST-L samples.

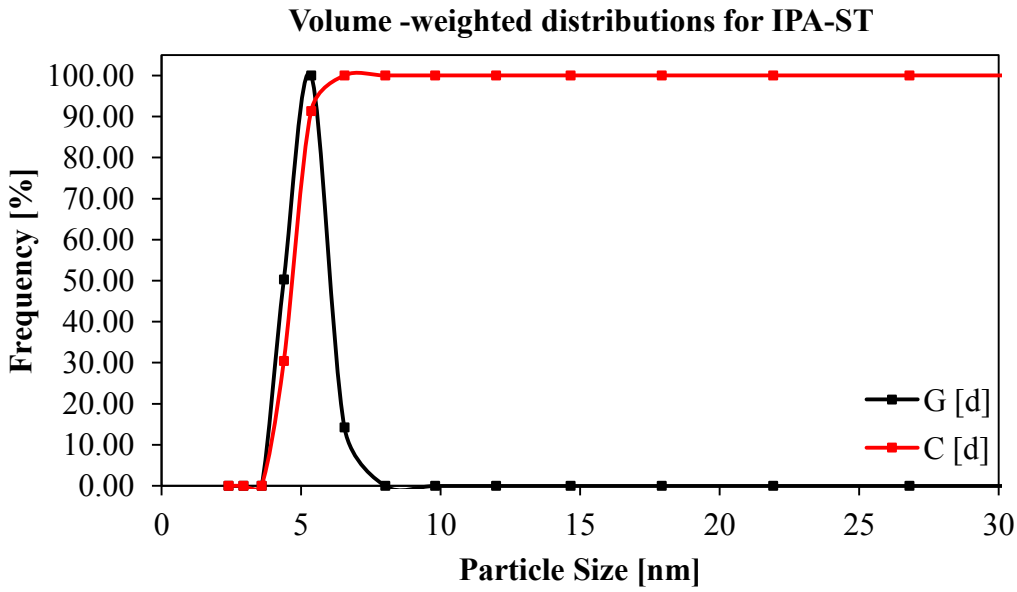

Figure 2.2 Volume-weighted differential and cumulative frequency distributions for IPA-ST colloidal silica dispersion suspension of silica nanoparticles. Concentration of silica nanoparticles was less than 0.1 wt% in dispersion.

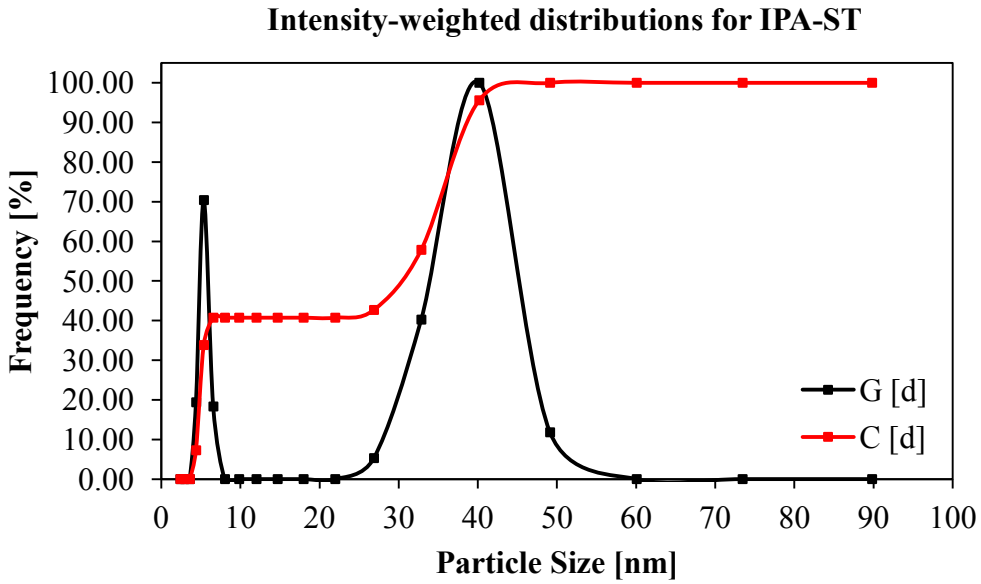

Figure 2.3 Intensity-weighted differential and cumulative frequency distributions for IPA-ST colloidal silica dispersion suspension of silica nanoparticles. Concentration of silica nanoparticles was less than 0.1 wt% in dispersion.

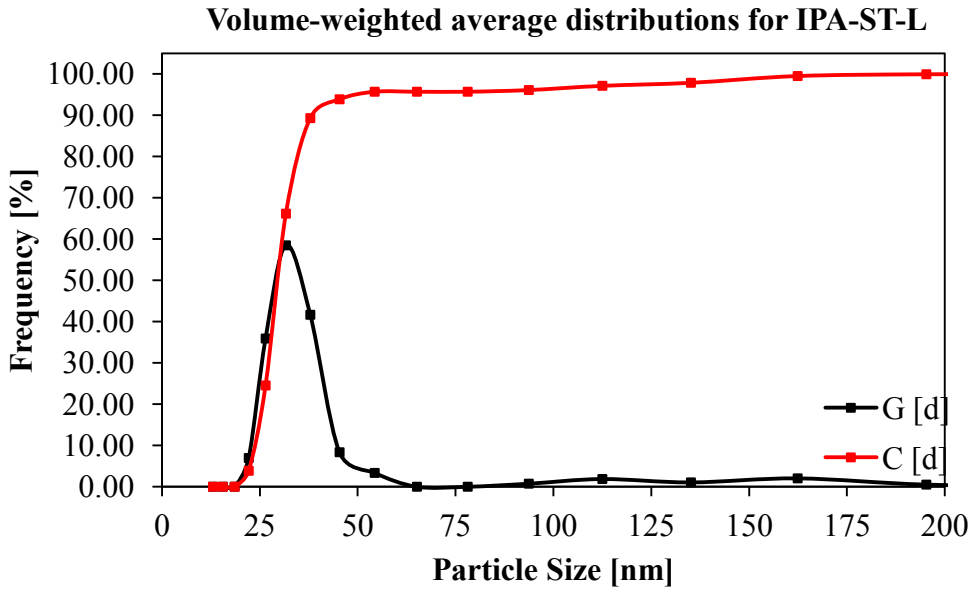

Figure 2.4 Volume-weighted differential and cumulative frequency distributions for IPA-ST-L colloidal silica dispersion suspension of silica nanoparticles. Concentration of silica nanoparticles was less than 0.1 wt% in dispersion.

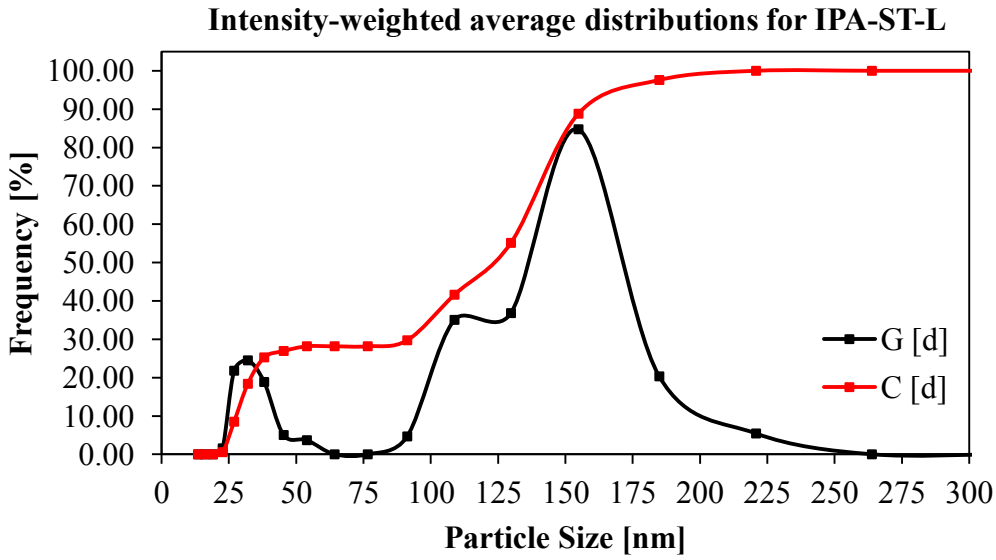

Figure 2.5 Intensity-weighted differential and cumulative frequency distributions for IPA-ST-L colloidal silica dispersion suspension of silica nanoparticles. Concentration of silica nanoparticles was less than 0.1 wt% in dispersion.

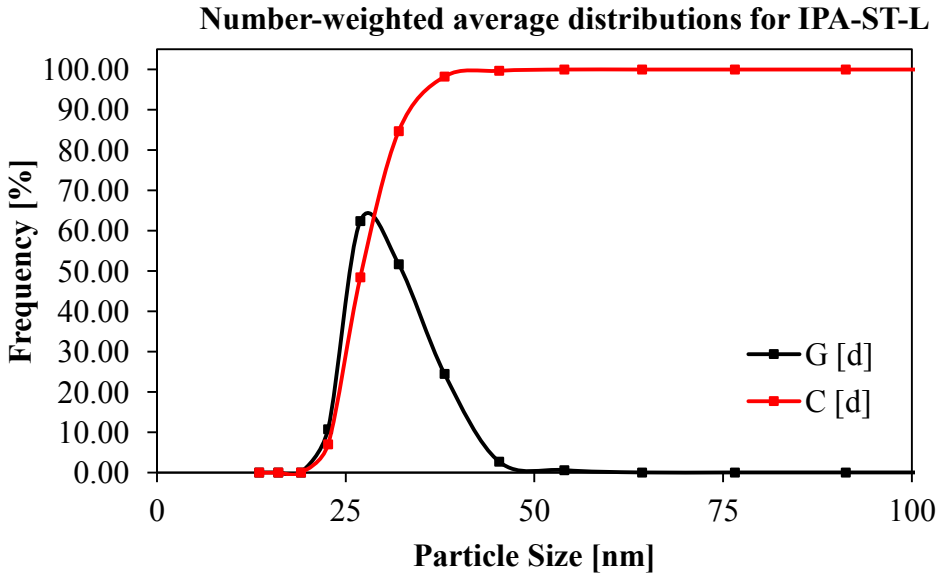

Figure 2.6 Number-weighted differential and cumulative frequency distributions for IPA-ST-L colloidal silica dispersion suspension of silica nanoparticles. Concentration of silica nanoparticles was less than 0.1 wt% in dispersion.

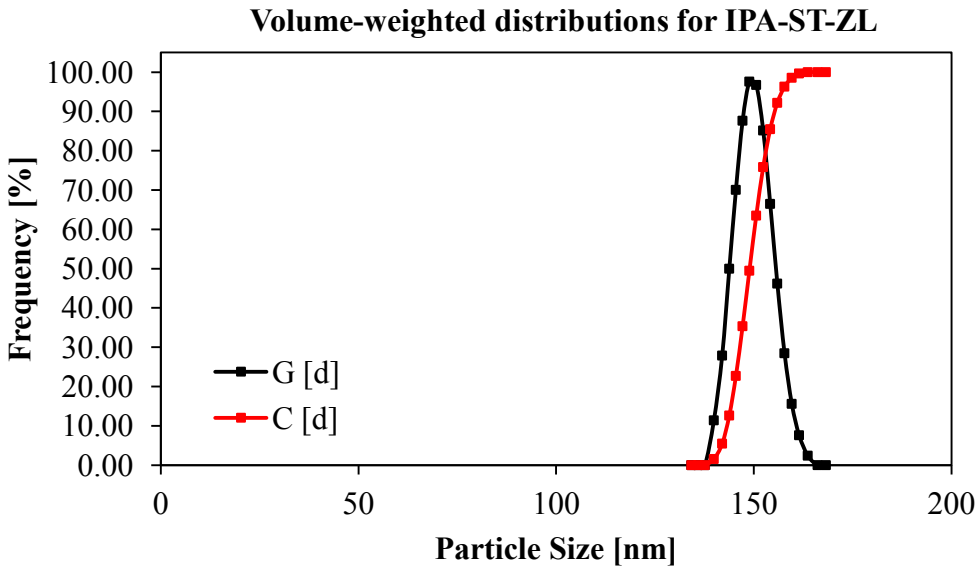

Figure 2.7 Volume-weighted differential and cumulative frequency distributions for IPA-ST-ZL colloidal silica dispersion suspension of silica nanoparticles. Concentration of silica nanoparticles was less than 0.1 wt% in dispersion.

Figure 2.7 shows the volume-weighted particle size distribution for IPA-ST-ZL colloidal silica. The particle size distribution is almost normally distributed. The average particle size was 148 nm with a range between 140 and 160 nm. The intensity and number-weighted particle size distributions were almost identical to the volume-weighted distribution. The particle size distribution of the SiO_2 nanoparticles for all type particle sizes showed monomodal distributions with averaged particle sizes inconsistent with manufacturer specifications.

Table 2.2 shows the average particle size for the three different size silica nanoparticles as reported by the manufacturer and obtained via dynamic light scattering. The standard deviation (σ_{DLS}), standard error (SE_{DLS}), and range are also shown in Table 2.2. DLS results provide the measured hydrodynamic particle size as described by Figure 2.1. Measurements for IPA-ST and IPA-ST-L particle sizes were much smaller when compared to manufacturer specifications. This is largely due to the fact that small particles scatter less light than larger particles. Heating caused by the laser used during the light scattering measurements could have affected the movement of the molecules. Evaporation of the isopropanol during measurement was also noticed. Possible carboxyl groups or small chain molecules could have present on the particles.

IPA-ST and IPA-ST-L samples were smaller than manufacturer reports. However, IPA-ST-ZL samples were much larger compared to manufacturer specifications. The manufacturer specifications are reported as 'typical'. Due to the range of particle sizes given by the manufacturer further investigation was necessary to know the materials which were used. Hence, it is imperative when obtaining any type of nano-material that the materials be characterized with multiple techniques to determine the particle size. Furthermore, since DLS does not provide primary particle size. TEM was also used to compare with manufacturer and DLS results. The intensity-weighted and number-weighted distributions are related to the volume-based distributions by Equations 2.7 and 2.8. Comparing these results to TEM results showed that the primary particle size distributions for all samples, ST, ST-L, and ST-ZL were log normally distributed and within manufacturer specifications.

Table 2.2 Shows the average particle size for the three different size silica nanoparticles as reported by the manufacturer and obtained via dynamic light scattering.

Organosilicasol™	$Size_{avg}$ [nm]				
Type	Manufacturer	DLS	σ_{DLS}	SE_{DLS}	Range
IPA-ST	10 - 15	5.36	0.034	0.015	4 -7
IPA-ST-L	40 - 50	31.6	2.79	1.25	22 - 45
IPA-ST-ZL	70-100	148.87	1.89	0.847	140 - 160

2.4 Transmission Electron Microscopy (TEM)

In correlation with using dynamic light scattering as a method to measure the particle size transmission electron microscopy can also be used to determine particle size, shape, and chemical makeup. TEM provides the primary particle size (exact particle diameter) in comparison to the hydrodynamic diameter, which tends to be larger, obtained using DLS. Images were taken using a JEOL 2010F TEM from JEOL Transmission Electron Microscopy, Japan. All samples of silica nanoparticles were diluted to a concentration less than 3 wt % then deposited onto a lacey carbon film with 200 mesh copper grids. The grids were from Electron Microscopy Sciences and dipped into dispersions, then allowed to dry in a vacuum to remove any solvent. Optimum magnification for all samples varied from 150K to 250K. Images were taken at 1024 × 1024 resolution for all samples. The cumulative distributions of the colloidal silica were determined using the TEM images and GIMP 2.8, a GNU image manipulation program. A random sample set of particles were numbered and measured according to pixel width then converted to a particle size using pixel to particle ratio.

2.4.1 Transmission Electron Microscopy - Results

Colloidal dispersions of diluted concentrations of silica nanoparticles in isopropanol were deposited onto a carbon lacey grid using a dip coating method, vacuum dried to remove all solvent residue, and then images of the particles were taken. Figure 2.8: A) Shows two TEM images of IPA-ST colloidal silica nanoparticles on a lacey carbon grid. B) Shows the raw data and lognormal particle size distribution obtained from multiple TEM images for IPA-ST. The particles were not aggregated or agglomerated.

The lognormal cumulative PSD was calculated using standard statistics after particles were measured using GIMP and a pixel to particle ratio was determined. Images were taken randomly throughout the lacey carbon grid to find the optimal images for measurement. The pixel-to-particle ratio was 0.333 nm per pixel for all images.

IPA-ST samples do contain a small amount of larger particles (greater than 15nm) which is the maximum reported by Nissan Chemical. The larger particles cause the distribution to be slightly wider than expected. The average particle size was 13.66 nm in diameter with a standard deviation of 2.96 nm and a standard error of 0.296 nm. The average particle size was within the range specified by the manufacturer.

A)

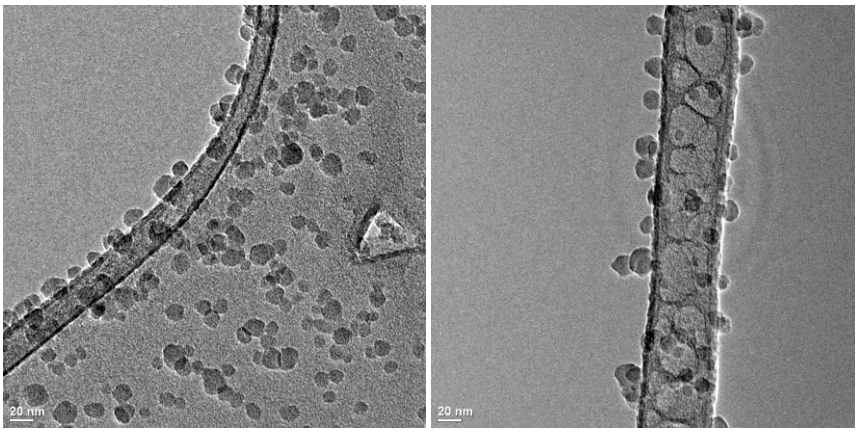

B)

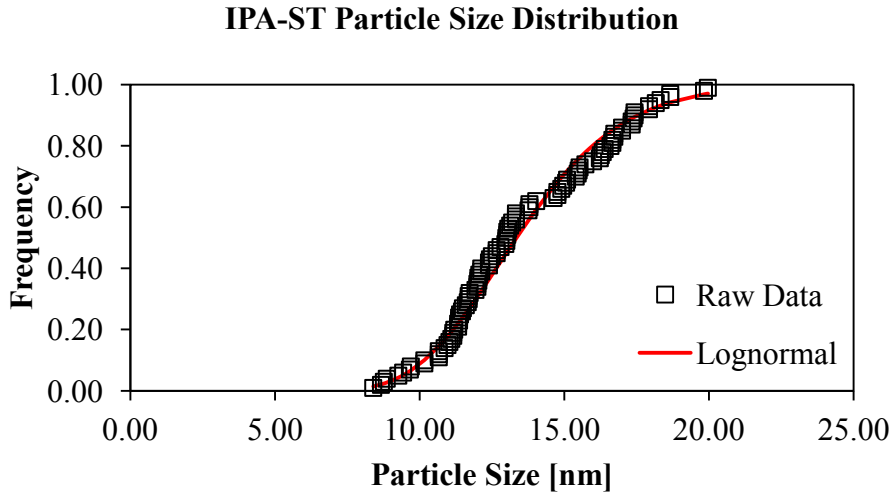

Figure 2.8 A) Shows two TEM images of IPA-ST colloidal silica nanoparticles on a lacey carbon grid. B) Shows the raw data and lognormal particle size distribution obtained from multiple TEM images for IPA-ST.

Table 2.3 shows three different distribution models (normal, lognormal, and Weibull distributions) which were tested to fit the raw data obtained via TEM. The arithmetic mean, standard error of the mean (SE_x), standard deviation (σ), standard error of the standard deviation (SE_σ), the r-squared value, and the inverserelative standard error of the mean or standard deviation ($RSE_x = SE_x$ / Mean or $RSE_\sigma = SE_\sigma$ / σ)are shown for each model fitted to the raw data. The lognormal distribution for IPA-ST in Figure 2.8 B has an average of 0.496 with a standard deviation of 0.299 and a standard error of 0.030. Distribution models tested showed the lognormal fit models the data the best out of all models tested and returned the highest RSE. The average primary particle size was within manufacturer specifications. These results will be later discussed in conjunction with the results from DLS.

Figure 2.9: A) Shows two images of IPA-ST-L colloidal silica on a lacey carbon grid B) Shows the raw data and lognormal particle size distribution obtained from multiple TEM images for IPA-ST-L. Like the particles in Figure 2.8, particles were not aggregated nor agglomerated in the TEM measurements.

The average particle size was 46.85 nm in diameter with a standard deviation of 7.04 nm and a standard error of 0.704 nm. The lognormal distribution for IPA-ST in Figure 2.9 B has an average of 0.495 with a standard deviation of 0.284, and a standard error of 0.028. It should be noted the first apparent image in Figure 2.9 A was significantly more concentrated than the image on the right. Areas throughout the lacey carbon grid did not necessarily contain a uniform number of particles. Because the particles were larger than IPA-ST a greater number of TEM images were needed to obtain the necessary data for the IPA-ST-L dispersion. The pixel-to-particle ratio varied between 0.333, 0.4, and 0.8333 nm per pixel. The lognormal distribution in Figure 2.9 B has an average of 0.51 with a standard deviation of 0.250, and a standard error of 0.029. Table 2.4 shows three different distribution models (normal, lognormal, and Weibull distributions) which were tested to fit the raw data obtained. Similarly to the IPA-ST particles, the lognormal model fit the data the best out of all models tested and returned the highest RSE. The average primary particle size was within manufacturer specifications.

Table 2.3 Models tested with fitted parameters for the raw data obtained during TEM.

Model	Mean	SE_x	σ	SE_σ	R^2	$[RSE_x]^{-1}$	$[RSE_\sigma]^{-1}$
Lognormal	2.723	0.003	0.191	0.004	0.985	*994*	48.22
Normal	15.35	0.033	2.774	0.052	0.987	408	52.97
Weibull	16.35	0.042	6.64	0.131	0.988	394	50.59

A)

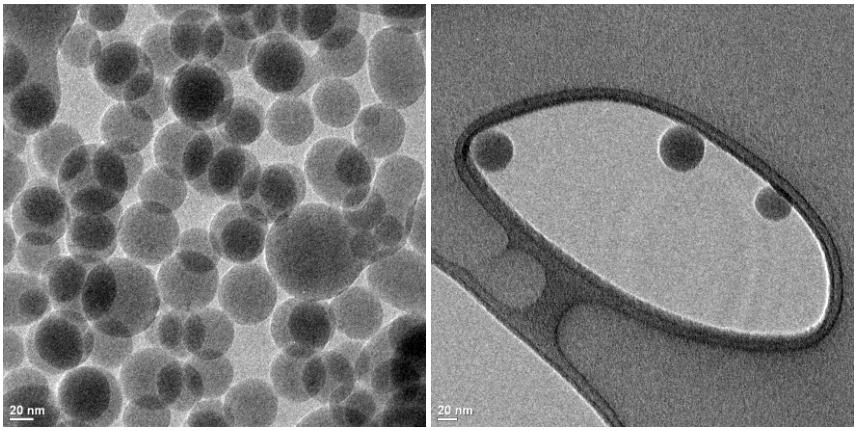

B)

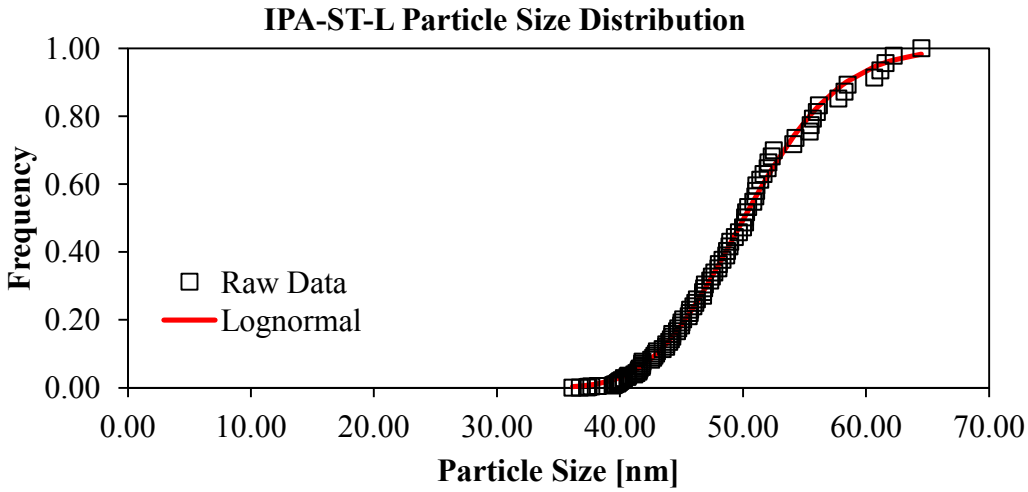

Figure 2.9 A) Shows two images of IPA-ST-L colloidal silica nanoparticles at two different concentrations dried on a lacey carbon grid. B) Shows the actual measured particle size fitted with a lognormal particle size distribution for IPA-ST-L measured on TEM.

Table 2.4 Shows three different models (normal, lognormal, and Weibull distributions) which were tested to fit the raw data obtained via TEM.

Model	Mean	SE_x	σ	SE_σ	R^2	$[RSE_x]^{-1}$	$[RSE_\sigma]^{-1}$
Lognormal	3.914	0.001	0.12	0.001	0.997	*5,210*	102.8
Normal	50.21	0.051	5.83	0.077	0.996	986	75.43
Weibull	52.26	0.105	10.38	0.242	0.987	499	42.96

Figure 2.10: A) Shows two images of IPA-ST-ZL colloidal silica nanoparticles dried on a lacey carbon B) Shows the raw data and lognormal particle size distribution obtained from multiple TEM images for IPA-ST-ZL. The particles were not agglomerated or aggregated in any of the images. The average particle size was 118.30 nm in diameter with a standard deviation of 7.00 nm and a standard error of 0.813 nm. The lognormal distribution for IPA-ST in Figure 2.7 B has an average of 0.51 with a standard deviation of 0.250, and a standard error of 0.029. The lognormal distribution in Figure 2.10 B did not fit the raw data (using calculated values not model values), as well as, the distributions in Figures 2.8 B and 2.9 B. This was due to both 'smaller' particles and 'larger' particles which could be possible outliers. Considering these data outliers, would greatly increase the fit of the lognormal distribution. Furthermore, the average particle size was larger than the range claimed by the manufacturer. Table 2.5 shows three different distribution models (normal, lognormal, and Weibull distributions) which were tested to fit the raw data obtained. Similarly to the smaller particles, the lognormal model fit the data the best out of all models tested and returned the highest RSE. The average primary particle size was larger than manufacturer specifications. Figure 2.11 shows the particle size distributions for all three different particle sizes measured via TEM with the lognormal model fitted to each respective distribution.

A)

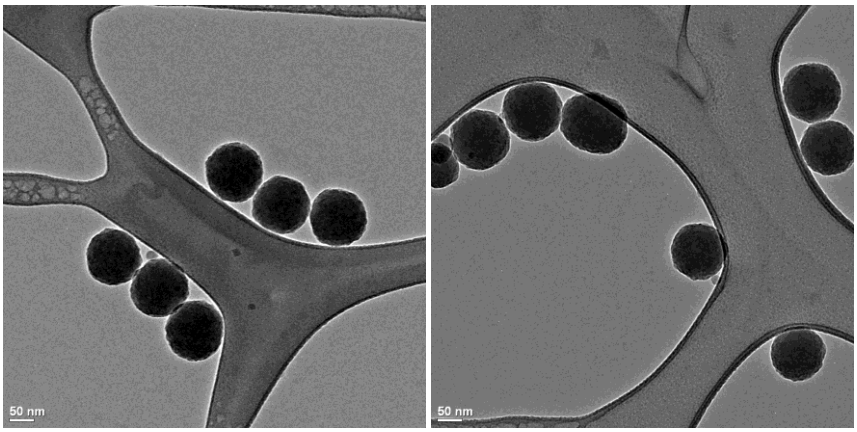

B)

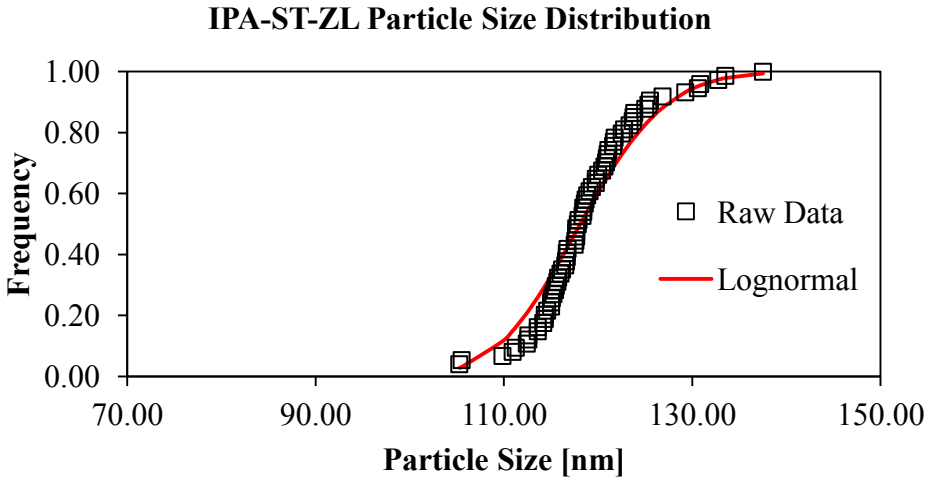

Figure 2.10 A) Shows two images of IPA-ST-ZL colloidal silica nanoparticles dried on a lacey carbon. B) Shows the actual measured particle size fitted with a lognormal particle size distribution for IPA-ST-ZL measured on TEM.

Table 2.5 Shows three different models (normal, lognormal, and Weibull distributions) which were tested to fit the raw data obtained via TEM.

Model	Mean	SE_x	σ	SE_σ	R^2	$[RSE_x]^{-1}$	$[RSE_\sigma]^{-1}$
Lognormal	4.797	0.001	0.037	0.001	0.992	*9,126*	45.52
Normal	121.1	0.068	4.387	0.103	0.991	1,788	42.52
Weibull	122.65	0.121	34.26	1.25	0.978	1,015	27.34

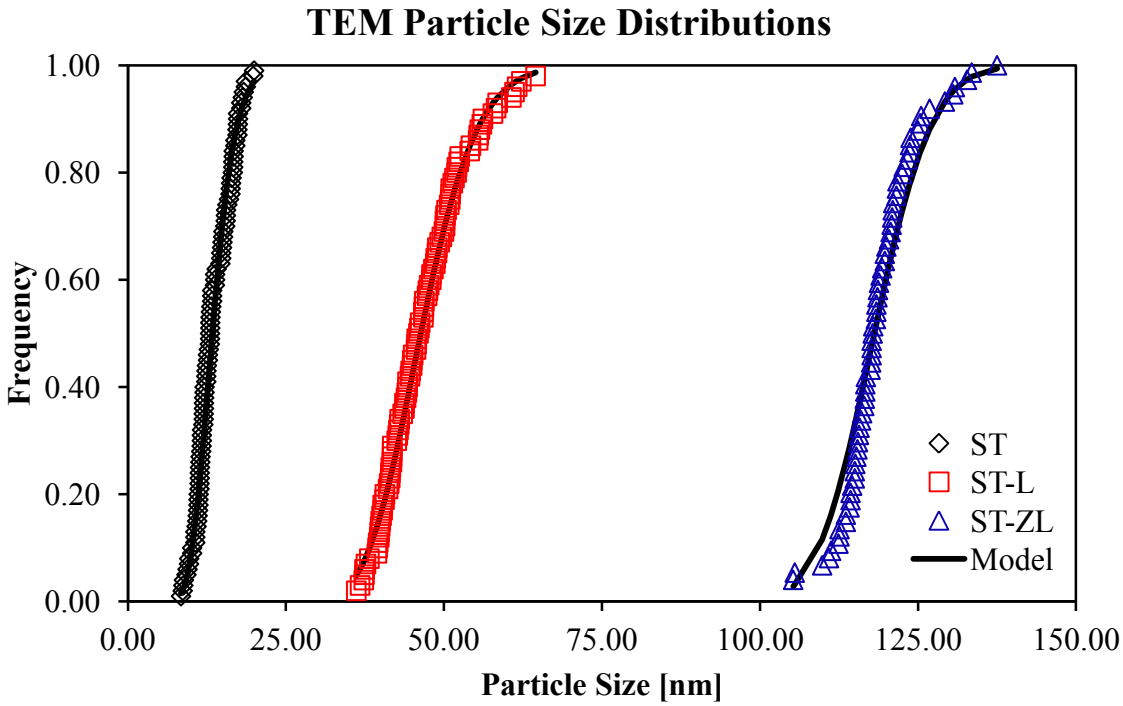

Figure 2.11 Cumulative master plot of particle size distributions with lognormal distribution model for all size particles determined using TEM.

2.5 Conclusions

The particle size distribution of three samples of ORGANOSILICASOL™ colloidal silica: IPA-ST (10-15), IPA-ST-L (40-50), and IPA-ST-ZL (70-100) was measured using DLS and TEM. The measured results were then compared with that reported by the supplier. Table 2.6 shows the average particle size reported by the supplier and obtained DLS/TEM measurements. The DLS measurement represents the grand mean and the standard deviation of the grand mean, while the TEM measurement represents the arithmetic mean and standard deviation of the particle sizes determined with each technique used. Figure 2.11 shows the particle size distributions for the TEM fitted with lognormal distribution models. The distributions are log normally distributed for all samples measured using TEM. The average primary particle size measurements obtained using TEM data was more consistent with the data supplied by the manufacturer than the data obtained using DLS. It should be noted that both DLS and TEM reported larger average particle sizes than the manufactures range for the IPA-ST-ZL colloidal solution.

The bimodal behavior found in the intensity-weighted data of IPA-ST and IPA-ST-L in Figures 2.3 and 2.5 was due to agglomeration of the particles at the conditions of the dispersion. Bimodal behavior was visible for the volume-based distribution of the IPA-ST-L sample. Volume-based distributions for IPA-ST and IPA-ST-ZL were unimodal. Although DLS data was not unimodal for all samples, the respective particle size distributions increased in size and breath as the particle size increased. This result was expected. Solutions were diluted but not sonicated before DLS scans were performed. The larger distributions of the samples suggest the affinity of the particles for one another in isopropanol under diluted concentrations. All particles remained dispersed in solution and therefore slight agglomeration is to be expected. Possible irregularity in the IPA-ST and IPA-ST-L samples during DLS measurements were most likely due to evaporation of isopropanol and possible carboxyl groups on the surface of the particles.

Dynamic light scattering techniques are measuring the movement of particles in dilute solutions and the particle size is an effective or hydrodynamic diameter measurement of the particles. The particle sizes determined using DLS was larger for IPA-ST-ZL particles and smaller for all other particles compared to TEM results.

Table 2.6 Average particle sizes measured by DLS and TEM compared with manufacturer specifications.

$Size_{avg}$ [nm]								
Type	Manufacturer	DLS	σ_{DLS}	SE_{DLS}	TEM	σ_{TEM}	SE_{TEM}	95% CI
IPA-ST	10 – 15	5.36	0.03	0.015	13.66	2.96	0.296	18-Oct
IPA-ST-L	40 – 50	19.16	2.79	1.25	46.85	7.04	0.704	41- 60
IPA-ST-ZL	70-100*	148.9	1.89	0.847	118.3	7.00	0.813	105 - 130

Moreover DLS provides the hydrodynamic diameter and TEM provides a primary particle diameter. This trend was also consistent with the TEM data. TEM results showed that all distributions of all different particles were log normally distributed and models fit the data very well. Furthermore, it is important to know the exact size and distribution of particles when trying to analyze the surface roughness of ultrathin nanocomposites. The particle sizes obtained from TEM analysis will be the values used throughout this document.

Chapter 3 Experimental and Analytical Methods

3.1 Introduction

Spin coating is most widely used in the microelectronics industry for the reproducibility and capability of producing a very thin uniform polymer film for photoresists [4]. Original studies conducted by Bornside, Macasko, and Scriven developed a one-dimensional model to predict the behavior of spin coating materials using spin coating [39]. Previous studies conducted by Stange, *et. al.* examined the effect of molecular weight and concentration of polystyrene thin coatings [40]. Furthermore, Hall et. al. presented one of the original studies on ultrathin polymer film thickness as a function of spin speed and polymer concentration [5]. Modeling of the overall film thickness, especially with the presence of nanoparticles, is difficult. The first stage of film thickness is governed highly by spin speed. The second portion of film thickness is governed by the rate of evaporation of solvent species. For purposes of this study the ultrathin coating thickness will assume to follow similar assumptions presented in previous studies.

Ultrathin film coatings are a growing area of research due to the capability to produce flexible coatings which are both hydrophilic and hydrophobic. A hydrophobic surface is not easily wetted by water, and similarly, a hydrophilic surface is easily wetted by water. The degree to which a surface is wetted describes the hydrophobicity or hydrophilicity of that particular substrate [41]. Superhydrophobic surfaces or coatings are defined as a surface whose water contact angle is greater than 150° [42, 43]. Superhydrophilic surfaces are defined as a surface whose water contact angle is less than 5° and are often referred to as being self-cleaning surfaces [44]. Superhydrophilicity is the property of a surface which is self cleaning, has anti-fog properties, or is biocompatible [42, 45, 46].

The wetting of a surface is highly dependent upon the relationships between the surface energies of the liquid and the surface energy of the substrate. Adhesion between the surface-liquid interface is governed by the forces between atoms. Atoms which are a couple of atoms in length below the surface have minimal contribution to the adhesion forces.

Researchers are developing more advanced types of coatings for hydrophobic and hydrophilic applications [42, 44, 47-49]. One of the most well-known examples of naturally occurring hydrophilic/hydrophobic surfaces is the lotus leaf which possesses self-cleaning properties obtained by the variances in the surface roughness on the nano- and micro-scales [50, 51]. By controlling the roughness of a surface, researchers can control the amount of interactions between the surface and it's interface depending on the phase and chemical makeup of the apparent interface. Changing the surface chemistry is one of the few other ways besides modifying the roughness to change the surface properties of a coating or surface.

3.2 Coating Materials

Glass substrates were chosen for simplicity, rigidness and hydrophilic surface properties. Precleaned Fisherbrand® microscope slides were obtained from Fisher Scientific. Two different methods were used to clean the microscope slides. Cleaning method 1 utilized distilled water with soap for an initial washing, followed by rinsing the slides a minimum of three times with isopropanol and drying between each rinse with compressed nitrogen. Cleaning method 2 utilized Fisherbrand® Sparkleen 1 as the initial hand washing agent, de-ionized-ultra-filtered (D.I.U.F.) water as the rinsing agent. Slides were then cleaned with 200 proof un-denatured ethanol obtained from Decon Labs Inc., rinsed with an acetone wash, and then washed with isopropanol. The isopropanol and acetone were obtained from Fischer Scientific®. Between each step the slides were dried with compressed nitrogen. This process thoroughly ensures that the slides are clean from organics and debris. Slides were stored in a sealed plastic container until ready to be coated. The best method was the second method previously mentioned. This provided a cleaner, spot-free surface. The method was compared visually and using AFM to examine the surface roughness.

Coating solutions were prepared using colloidal silica from Nissan Chemicals using three different size nanoparticles: IPA-ST (10-15), IPA-ST-L (40-50), and IPA-ST-ZL (70-100). The acrylate monomer dipentaerythritolpentaacrylate (SR399) purchased from Sartomer USA, LLC. was used for its clarity, abrasion resistance, flexibility with hardness, fast curing response for ultraviolet light, and low skin irritation. The initiator, 1-Hydroxy-cyclohexyl-phenyl-ketone (Irgacure 184) from Ciba Specialty Chemicals, was used for its efficient non-yellowing properties during photopolymerization of unsaturated prepolymers (in particular acrylates). Isopropyl alcohol 99+% was purchased from Fischer Scientific.

3.3 Ultrathin Nanocomposite Film Recipes

In order to obtain an ultra-thin nanocomposite film, high sheer rates and low viscosity fluids are needed. The film recipes were developed by spin coating a low viscosity fluid at high speeds to promote quick evaporation of the solvents, leaving behind a polymer-particle sol-gel matrix to be cured. The mixtures were comprised of solids and liquids. The solids were dipentaerythritolpentaacrylate (SR399), silica nanoparticles, and Irgacure 184; the liquids were isopropanol and 1-methoxy-2-propanol alcohol.

Original concentrations were determined to be: IPA-ST was 32.93 wt% silica nanoparticles, IPA-ST-L was 37.34 wt% silica nanoparticles, and IPA-ST-ZL was 35.67 wt% silica nanoparticles. Three dilutions for all three different size colloidal silica were prepared. Table 3.1 shows the concentrations of the diluted colloidal dispersions. A stock solution of 5 wt% SR399 in 1-methoxy-2-propanol was also prepared. The stock solution was then used as needed with the addition of 3 wt% initiator (based on monomer only) before precursor solutions were prepared. Each diluted colloidal silica solution was then mixed in a 1:1 weight ratio with the monomer solution to produce spin coating precursor solutions. Table 3.2 shows the final concentrations of silica in all of the different spin coating solutions for each respective size silica nanoparticles.

Coatings were then prepared using a novel spin coating system with a spin speed of 1255 revolutions per minute (RPM). Figure 3.1 shows the calibration of the in-house spin coater using a Monarch RPM measurement gun. Monomer solutions were then applied using a squeeze bulb pipet with approximately 1-2 mL of monomer precursor solutions. Figure 3.2 A) Shows the in-house spin coating system used to produce the ultra-thin film nanocomposite coatings. Once applied, glass slides remained in revolution for 5 seconds. Figure 3.2 B) Shows the White Lightning 3200X Flash Unit from Paul C. Bluff, Inc. used to cure the ultra-thin nanocomposite coatings. The coatings were flashed three times with a 250 Watt bulb waiting 5 seconds between each UV flash. Flash times were 1/300 seconds.

Table 3.1 Concentrations of diluted colloidal silica samples in IPA.

IPA-ST [wt%]		IPA-ST-L [wt%]		IPA-ST-ZL [wt%]	
Calculated	Actual	Calculated	Actual	Calculated	Actual
3	2.81	3	2.82	3	2.84
9	7.60	9	7.84	9	7.73
15	11.48	15	11.97	15	11.84

Table 3.2 Concentrations of silica in colloidal dispersions for spin coating.

Silica concentrations for 1:1 wt:wt Mixtures for precursor solutions		
IPA-ST [wt%]	IPA-ST-L [wt%]	IPA-ST-ZL [wt%]
1.41	1.41	1.42
3.79	3.91	3.87
5.74	5.99	5.92

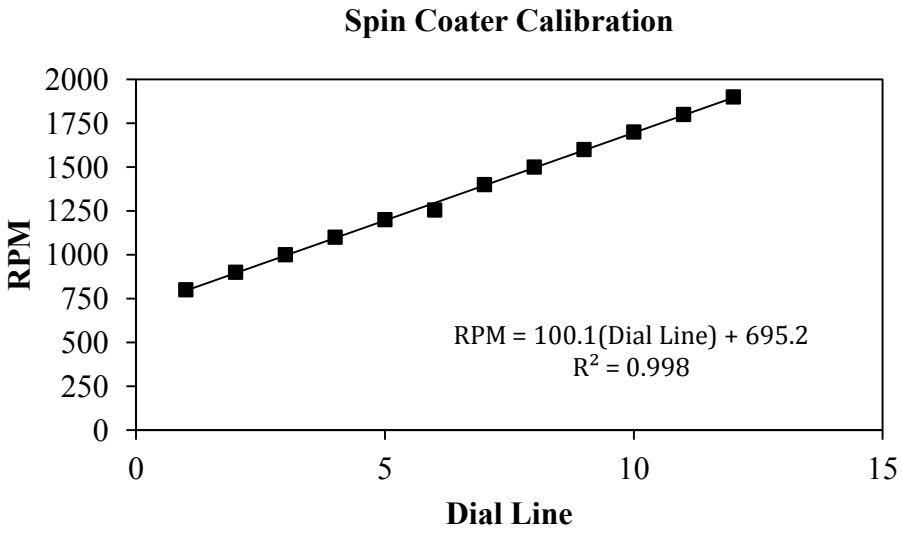

Figure 3.1 Shows the calibration plot for the in-house spin coating system found in Figure 3.2 A.

A) B)

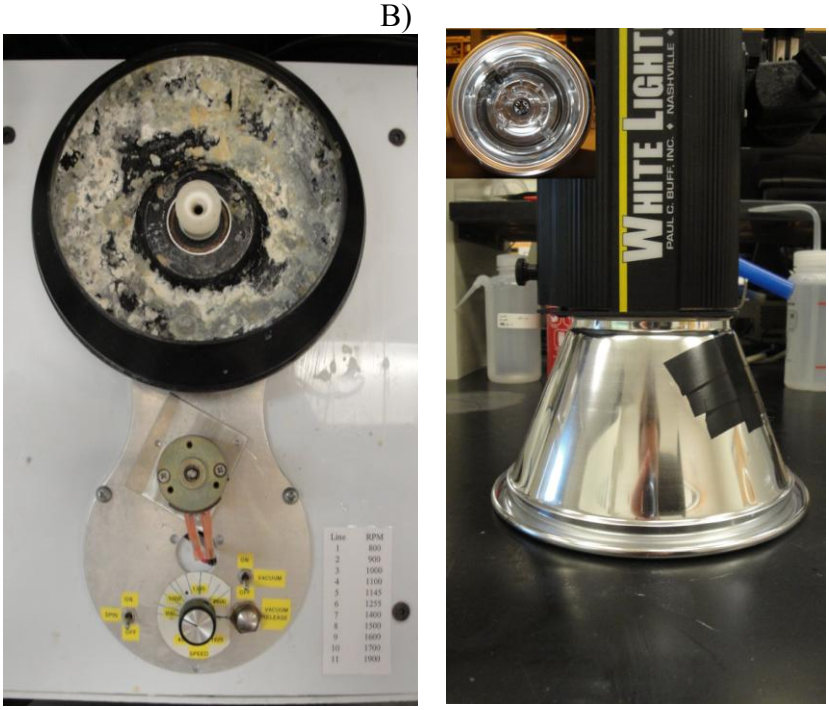

Figure 3.2 A) Shows the “in house” spin coating system used to make the ultra-thin film coatings. B) Shows the White Lightning UV source used to cure the coatings.

3.4 Profilometry Measurements

A Veeco Dektak 6M Stylus Profilometer was used to measure and verify the thickness of the ultra-thin film nanocomposites for multiple samples. Single layer film coatings ranged from 120 to 170 nm film thickness depending on the particle size. Smaller silica particles resulted in a thinner film coating while larger particles resulted in thicker film coatings. Double layer film coatings ranged from 300 to 450 nm in film thickness. Samples were prepared using a standard razor blade to delaminate a section of the film from the glass substrate. The profilometer measures the variance in height along a single axis using a diamond stylus. Scan rates were maintained 100 μm per second. The total scan distance was 5 mm. Sample positioning had no effect on the outcome of the data. This was established by measuring the surface thickness over multiple positions of the sample in the horizontal, vertical, and diagonal axis.

Figure 3.3 shows two examples of the profilometer scans obtained - a single and double layer ultra-thin film coating. Figure 3.3 A) shows a single layer coating which has a coating thickness approximately 150 nm. All single layer coatings ranged between 120 and 170 nm. Figure 3.3 B) shows a double layer coating which has a coating thickness approximately 350 nm. Again, all double layer coatings ranged between 300 and 450 nm. The profilometer is a very efficient and quick way to obtain the variance in height along a single axis. For a more exact measurement of the coating thickness the sample should be cast in a resin and a cross section should be observed using TEM. This method is very timely and cost inefficient. Limitations include the resolution of the data and the inability to efficiently obtain three dimensional topographic data. Atomic force microscopy will be used to determine the topography as opposed to using profilometry.

A)

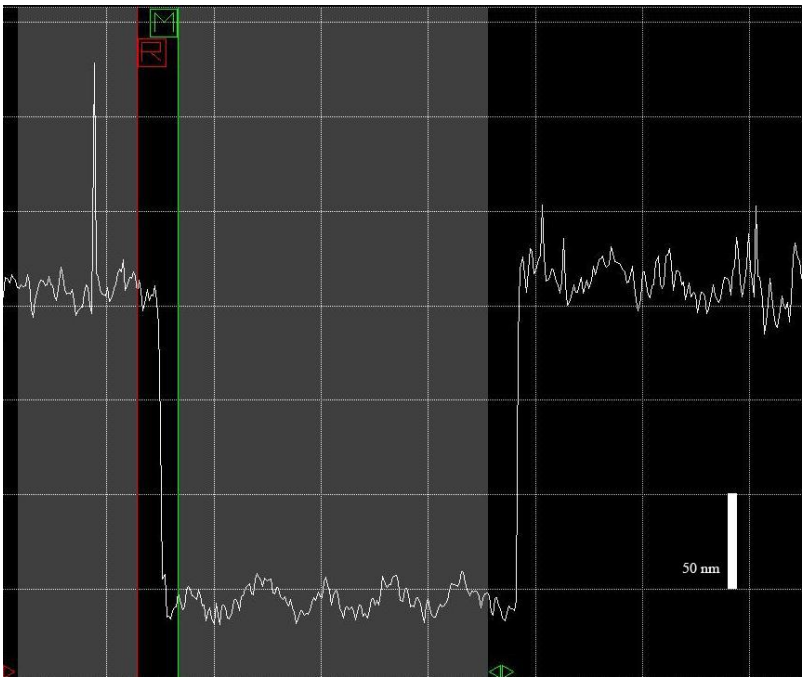

B)

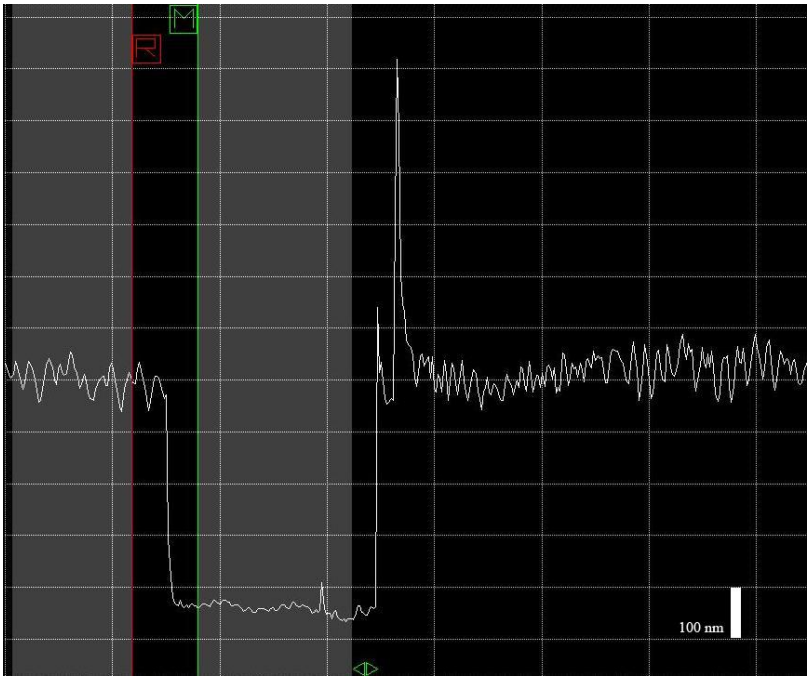

Figure 3.3 Profilometry scans of A) single layer ultra-thin film coating. B) double layer ultra-thin film coating. Calibration bar is equal to 50 nm for A and 100 nm for B.

Chapter 4 Atomic Force Microscopy - Experimental

4.1 Introduction

All coating samples prepared were analyzed using an Agilent Technology AFM model no. 5500 with isolation chamber. Non-contact mode / tapping mode, was used with a large area scanner with a scan range 1μm × 1μm to 100μm × 100μm. In particular the small area scanner (scan range from 0.1μm ×0.1μm to 10μm × 10μm) was not used due to the limitations of the scanner when approaching the limits of the scan range. Scan sizes for samples between 5μm × 5μm, 10μm × 10μm, and 25μm × 25μm. Scans taken at the 10μm × 10μm sample size were used for comprehensive analysis with a resolution of 512 × 512 pixels. Tap 300Al-G cantilevers were purchased from Ted Pella, Inc. and manufactured by Budget Sensors with a resonant frequency of 300 kHz, force constant of 40 N/m, and aluminum reflex coating. Figure 4.1 shows the basic principle of how the topographic three dimensional surface is constructed using the AFM cantilever tip. The tip 'drags/taps' across the surface of a material and a detector measures the intensity in the deflection of the laser. The signal is then converted to a three dimensional topographical image using the provided software, Agilent Technologies Picoview 1.10.1. However, Picoview does not have the most appropriate data analysis capabilities. Raw data was saved and processed using Gwyddion.

Gwyddion v2.31, a scanning probe microscopy (SPM) image analysis program was used to process all raw data obtained from AFM. Data manipulation steps included but did not necessarily require the following: Fix zero, level data by mean-plane subtraction, remove scars / correct horizontal scars (strokes), line correction / correct lines by matching height median, shade data, and statistical quantities. Various combinations of data manipulation steps were used to obtain the most realistic representation of the raw data. The root mean square (RMS) roughness was then obtained for each sample.

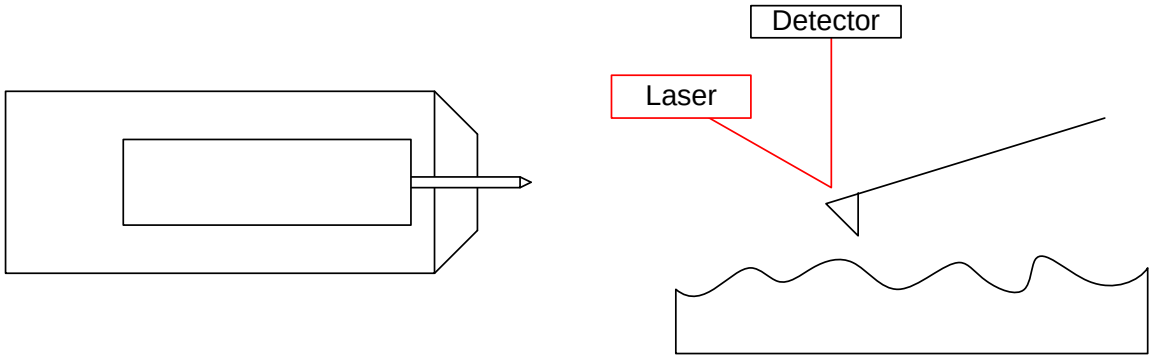

Figure 4.1 Shows an example of the design of the AFM cantilever tip used and the basic concept design concept of AFM operation. The laser reflects off the surface of the cantilever and is recorded by the detector while drug across a surface.

4.2 Surface Roughness

The RMS roughness is the average of the measured height deviations taken within the evaluation length and measured from the mean line of a sample (Gwyddion manual). This follows ASME B46.1-1995, ISO 4287-1997, and ISO4287/1-1997 standards. The root mean square (RMS) roughness, R_q, is calculated as shown by Equation 4.1.

$$R_q = \sqrt{\frac{1}{N}\sum_{j=1}^{N}(z_j - \bar{z})^2} \qquad \text{Equation 4.1}$$

Where R_q, N, z_j, and $\bar{z}$ are the root mean square roughness, sample size, height of each data point collected, and average height, respectively. The surface roughness is solely dependent upon the height distribution of the peaks within a sample.

4.3 AFM for Glass and Neat Polymer Mixture

Before the surface coating mixtures were applied, the surface analysis was performed on pure glass substrate samples and neat polymer. The initial measurements conducted using AFM were performed on the glass substrates to verify the initial surface roughness of the material coated. Figure 4.2 shows two 10×10 um scans of two different glass samples. Figure 4.2 A) shows the glass substrate surface topology after using cleaning method 1. Figure 4.2 B) shows the glass substrate surface topology after using cleaning method 2. This experiment was performed to determine which cleaning method previously mentioned was the best for the substrates used. The surface roughness was measured for both samples with R_q = 5.1 nm and 2.9 nm respectively for cleaning method 1 and cleaning method 2. This verifies that cleaning method 2 was better for removing debris and organics from the surface. Cleaning method 2 was used for all glass substrates for all samples. A series of measurements were made using multiple scans to obtain an average substrate surface roughness with R_q = 3.59 nm with a standard deviation, σ = 0.65 nm. It is imperative to minimize the time exposing substrates to the atmosphere before and after coating since dust and particles can adhere to the surface via static energy. As seen in Figure 4.2 B there are a few dust particles on the surface, the largest being in the top corner with a height of 107 nm.

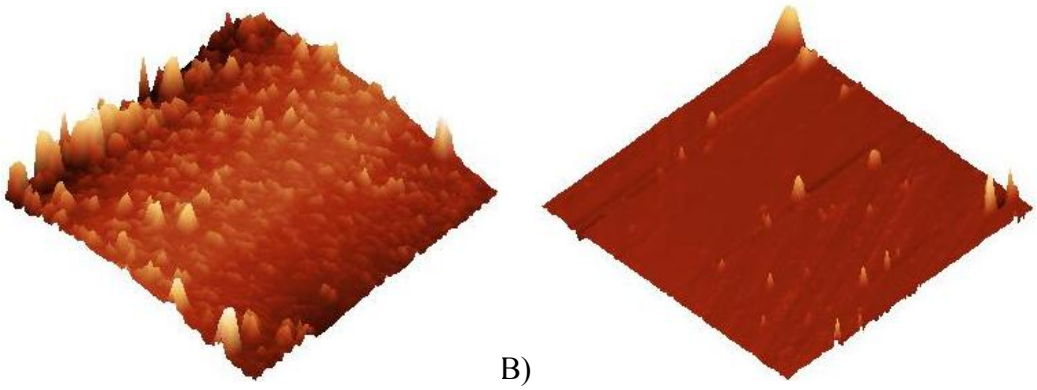

A) B)

Figure 4.2 Shows two 10 × 10μm scans of two different glass samples. A) was cleaned using cleaning method 1. B) was cleaned using cleaning method 2.

Figure 4.3 Shows two 5 × 5μm AFM scans of neat polymer coatings. Figure 4.3 A is a single layer coating of neat polymer shown with a few minor imperfections. The image with imperfections was chosen to show a difference in height on the surface. These imperfections are largely due to dust contamination of the particular sample. No silicon nanoparticles were present in the mixture used to coat the glass slide. Figure 4.3 B is similar to Figure 4.3 A, a double layer coating of neat polymer again shown with a minor imperfection. It should be noted that Figure 4.3 B has only one major imperfection and Figure 4.3 A has four major imperfections. Visualizing the topography of ultra-thin polymer coatings without imperfections can be difficult as can be seen in the areas without imperfections in both Figure 4.3 and Figure 4.4. This is due to the surface being extremely uniform and indifferent over the substrate. A large amount of debris/dirt is covered and the static of the surface decreases, leaving an extremely uniform coating. Figure 4.4 shows the vertical view of both respective images in Figure 4.4. Single coatings were approximately 150 nm and double layer coatings were approximately 300 nm. A series of measurements were made using multiple scans for both the single and double layer coatings. The average single layer surface roughness was R_q = 1.09 nm with a standard deviation, σ = 0.36 nm. The average double layer surface roughness, R_q = 0.69 nm with a standard deviation, σ = 0.06 nm.

Figure 4.5 shows the difference in average surface roughness between glass, a single layer polymer coating, and a double layer polymer coating. The decrease in surface roughness is a direct result of the uniformity which the polymer layer forms during the spin coating process. The ultrathin film polymer coating is extremely smooth due to the low viscosity of the monomer mixture allowing monomer to fill any gaps or valleys on the surface of the substrate. Figure 4.5 also shows applying a second ultra-thin film coating upon the first slightly decreases the surface roughness. The error bars represent the standard deviation (of the grand mean) for each respective type of coating. Furthermore, there is not a large variation in the difference between a single layer and a double layer coating of the neat polymer. This goes to show that the surface roughness would not change significantly if additional layers are applied. If additional layers were applied the surface roughness would be very close to that of the double layer coating surface roughness.

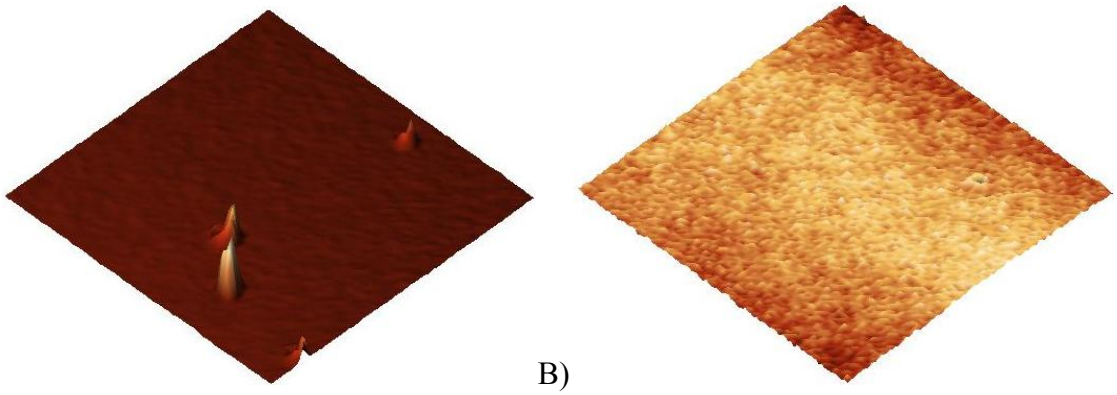

A) B)

Figure 4.3 Shows two 5 × 5μm AFM scans of neat polymer coatings A) A single layer coating of polymer mixture without nanoparticles (thickness ~ 150 nm). B) A double layer coating of polymer mixture without nanoparticles (thickness ~ 300 nm).

A) 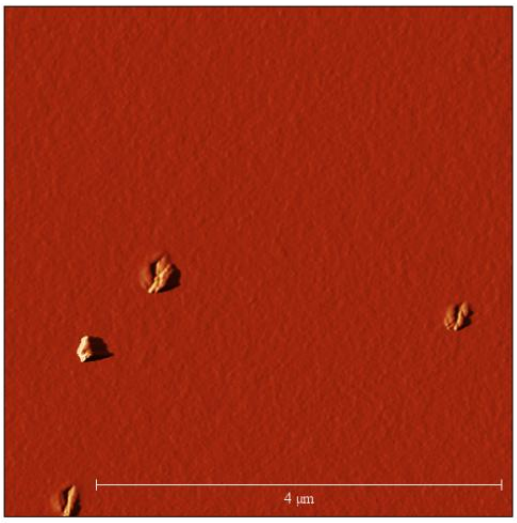

B) 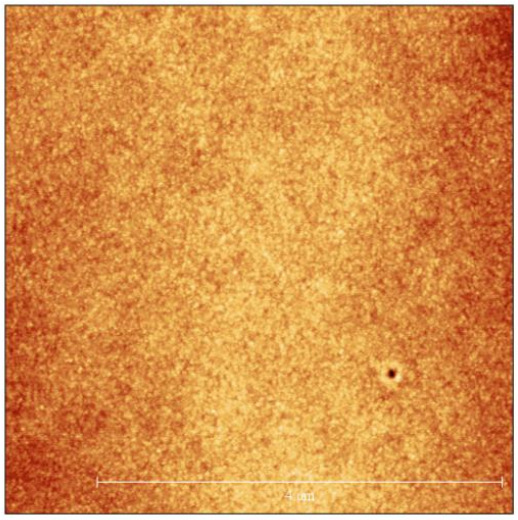

Figure 4.4 Shows the vertical topography image of the three dimensional images found in Figure 4.3. A) Shows the single layer coating of neat polymer on glass B) shows the double layer coating of neat polymer on glass.

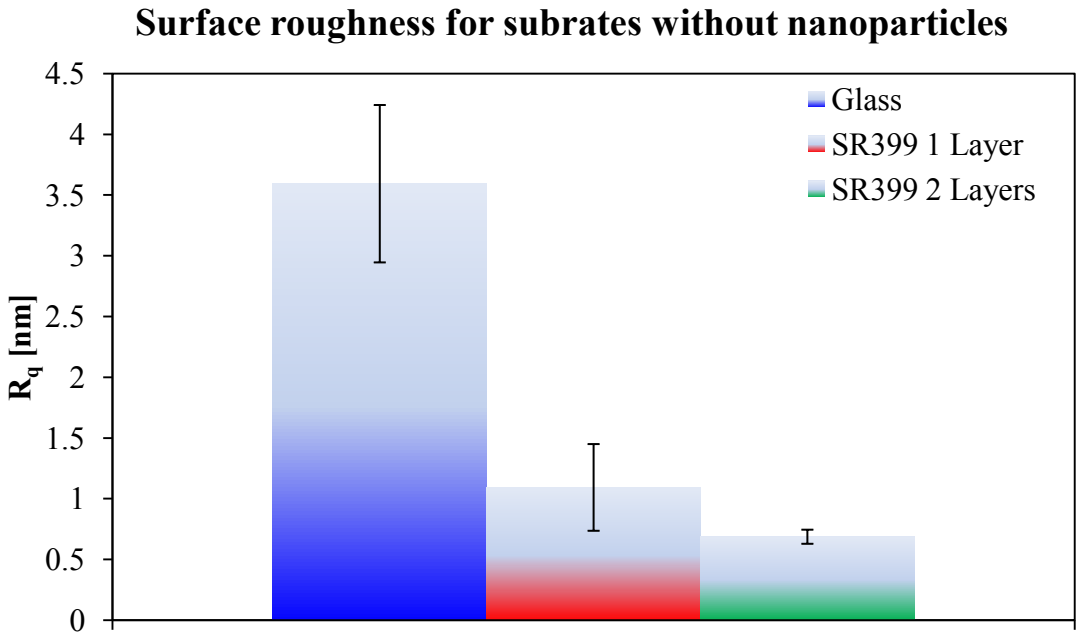

Figure 4.5 Comparison of average surface roughness for glass, neat (without particles) single coating and neat double coating ultra-thin film coatings. Error bars represent the standard deviation of the grand mean.

4.4 AFM of Colloidal Silica Nanocomposites

The surface roughness of colloidal silica nanocomposites was then compared to that of the glass, single layer polymer coatings, and double layer polymer coatings. The nanocomposites were coated in the same manner as previously described. Three different concentrations of particles were used for each size nanoparticle. Single and double layer nanocomposites were also examined for each concentration. The surface roughness for different nanocomposite formulations was then compared for each particle size.

4.4.1 IPA-ST-L Nanocomposites

Nanocomposite film coatings with IPA-ST-L particles were prepared and analyzed. Single and double layer coatings were prepared with concentrations of 1.41, 3.91, and 5.99 wt% silica nanoparticles in monomer dispersions. Three measurement scans were performed for each different scan size: 5 × 5 μm, 10 × 10 μm, and 25 × 25 μm for each sample. Table 4.1 shows the matrix of surface roughness measurements used to determine if variation in surface roughness exists with different scan sizes of the same surface. Three measurements were taken for each scan size for each concentration silica nanoparticles. All groups of three scans were performed on random places on the same surface for each respective sample.

Surface roughness values for both single and double layer coatings were compared to one another using analysis of variance (ANOVA) statistical analysis. A confidence level of $\alpha = 0.05$ was used. Table 4.2 shows the p-value and F-test values from ANOVA comparing the differences in surface roughness measurements between scan sizes (5 μm vs. 10 μm vs. 25 μm) for each concentration of silica nanoparticles for single layer and double layer coatings independent of one another. Only the double layer 1.41 wt% silica nanocomposite film returned a p-value less than 0.05 (0.048) with F-value greater than F-critical value (5.232 > 5.1432). As ANOVA test results met the null hypothesis, (that there was no significant difference between surface roughness and scan size), a scan size of 10 × 10 μm was used for universal analysis for all samples.

Table 4.1 Matrix of surface roughness measurements used to determine if variation in surface roughness exists with different scan sizes of the same surface. Weight percent is the concentration of silica in dispersion mixtures.

		1.41 wt% SiO_2 (20 vol % solids)	3.91 wt% SiO_2 (40 vol % solids)	5.99 wt% SiO_2 (50 vol % solids)
1 Layer				
Scan size [um]	**Scan**	**R_q [nm]**	**R_q [nm]**	**R_q [nm]**
5	1	11.0	13.6	18.0
	2	12.8	13.1	14.8
	3	12.3	15.6	15.3
10	1	11.3	14.0	18.7
	2	13.0	14.6	19.7
	3	12.2	13.3	15.8
25	1	13.7	12.1	20.5
	2	10.7	16.9	19.2
	3	9.80	15.9	20.1
2 Layers				
5	1	13.6	14.2	14.3
	2	13.9	12.3	16.0
	3	14.1	12.3	18.4
10	1	15.6	13.9	18.0
	2	15.4	12.5	25.9
	3	16.6	12.1	22.7
25	1	14.8	11.7	21.6
	2	10.4	10.6	54.0
	3	11.4	11.4	25.8

Table 4.2 p-values and F-test statistics from ANOVA analysis of R_q for IPA-ST-L nanocomposite films for multiple scan sizes to determine significance of scan size for each respective concentration.

Single Layer (α = 0.05)			
Concentration	P-value	F	F crit
1.41	0.550	0.662	5.1432
3.91	0.745	0.309	5.1432
5.99	0.063	4.559	5.1432
Double Layer (α = 0.05)			
Concentration	P-value	F	F crit
1.41	*0.048*	*5.232*	*5.1432*
3.91	0.104	3.384	5.1432
5.99	0.195	2.173	5.1432

ANOVA test were also performed between two groups of data (5μm vs. 10μm, 10μm vs. 25μm, 5μm vs 25μm). When comparing only two groups of data the ANOVA test becomes a two-tailed t-test, assuming the variances are equal between groups (homoscedastic). The p-values can be found in Appendix B. Since the data sets are small it is difficult to validate using the ANOVA (t-test) for comparison between only two groups with such small sample size.

The data obtained using AFM in Table 4.1 was then restricted to the 10 × 10 μm samples only. Figure 4.6 shows the 3-D scans for the respective weight concentration of IPA-ST-L silica nanoparticle dispersions. A, C, E are single layer coatings; B, D, F are double layer coatings. All scans were performed with a 10 μm × 10 μm scan size. The concentration of silica is indicated below each image. Differences in color are typically a result from instrument alignment, signal strength, and differences in the delta z-height. Shading/lighting can be applied if the same color aspect is desired, however not necessary. Double layer coatings are independent of single layer coating experiments (i.e. the double layer coating was not made from the single layer coating).

Table 4.3 shows the delta z-height difference and surface roughness values for each respective image in Figure 4.6. As delta-z increases the surface roughness will typically increase, resulting from greater variation between the maximum and minimum peaks within a sample scan. There is no direct correlation between surface roughness and delta-z values for a sample. The surface topology of single film nanocomposites visually appear to be rougher than double layer nanocomposite films which would follow the same trend as coatings without particles. Furthermore, it is apparent that there is a difference in the surface topology as a function of the concentration of silica.

The three surface roughness measurements for each sample were averaged and reported for both single and double layer coatings. Figure 4.7 shows the averaged root mean square roughness for single and double layer coatings for the respective weight percent silica in dispersion. Final concentrations of silica in the nanocomposite films (based on solids only) were 35 wt% (20 vol%), 60 wt% (41 vol%), and 70 wt% (51 vol%) for the respective increasing concentrations of colloidal dispersions – 1.41, 3.91, and 5.99. The 20 vol. % sample produced an average R_q = 12.17 nm (σ = 0.85 nm) and

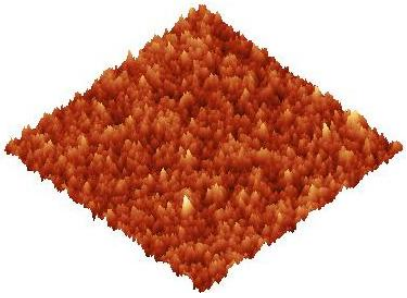

A) 20vol % 1 Layer

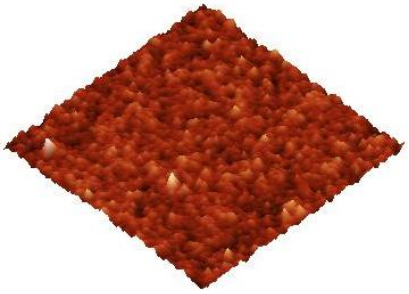

B) 20 vol % 2 Layers

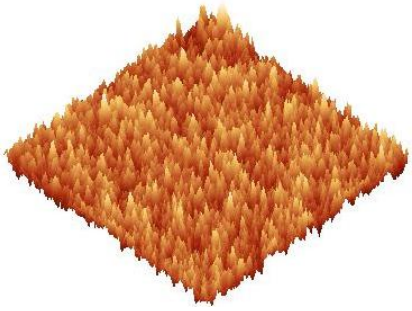

C) 41 vol % 1 Layer

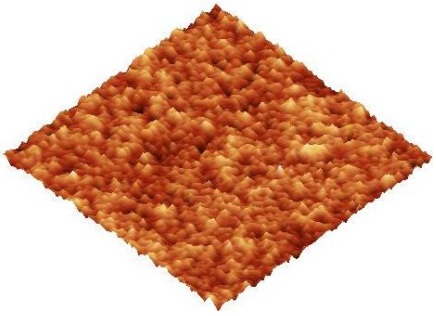

D) 41 vol % 2 Layers

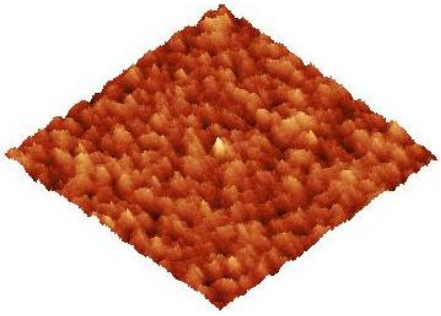

E) 51 vol % 1 Layer

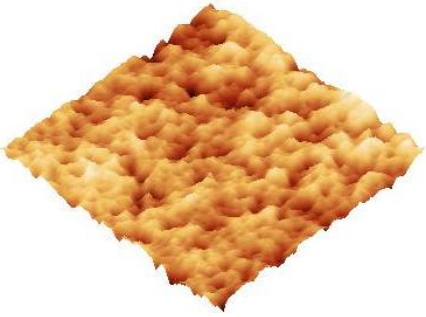

F) 51 vol % 2 Layers

Figure 4.6 Shows the 3-D scans for the respective volume concentrations of IPA-ST-L silica nanoparticle nanocomposites. A, C, E are single layer coatings; B, D, F are double layer coatings. All scans were performed with a 10 μm x 10 μm scan size.

Table 4.3 Shows the surface roughness values and the height differential values for each respective figure in Figure 4.6.

Figure	Δ Z height [μm]	R_q [nm]
A	0.12	11.3
B	0.20	15.4
C	0.13	14.0
D	0.11	12.1
E	0.17	15.8
F	0.24	26.0

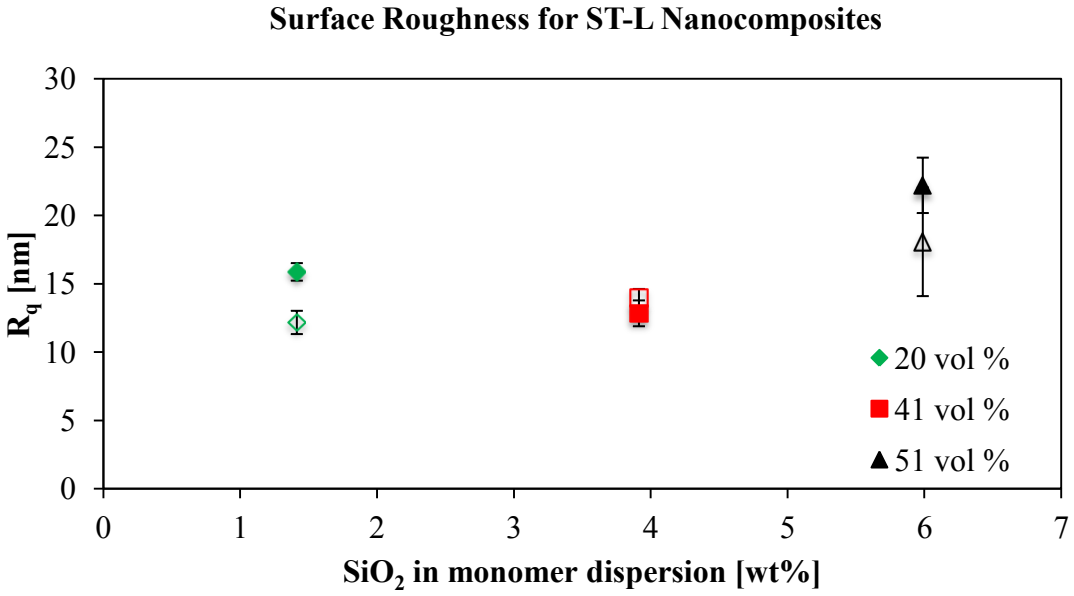

Figure 4.7 Average surface roughness for single and double layer IPA-ST-L nanocomposite coatings. Open symbols are single layer films. Closed symbols are double layer films. The volume percentage of silica in the solid films is also indicated.

R_q = 15.87 nm (σ = 0.64 nm) for single and double layer nanocomposites, respectively. The 41 vol. % sample produced an average R_q = 13.96 nm (σ = 0.65 nm) and R_q = 12.83 nm (σ = 0.95 nm) for single and double layer nanocomposites, respectively. The 51 vol. % sample produced an average R_q = 18.06 nm (σ = 2.03 nm) and R_q = 22.2 nm (σ = 3.97 nm) for single and double layer nanocomposites, respectively. The surface roughness, R_q, is fairly consistent from 20 to 51 volume percent, but variation in R_q does increase as the particle loading increases. The variation is represented by the error bars (± grand mean standard deviation). As the particle loading increases the surface roughness follows an increasing trend, but does not vary significantly.

Both the smallest and largest concentration silica nanoparticle loading (20 vol% and 51 vol%) showed a slight increase in surface roughness as the second layer of deposition was measured. The film with 41 vol% loading shows a slight decrease in surface roughness compared to the single film coating, which was unexpected. This irregularity in the surface could have been caused by numerous factors including, but not limited to: temperature during deposition leading to varying solvent evaporation rates, contaminated AFM tip causing incorrect measurement, or less particle loading for the given area that was scanned. For IPA-ST-L film coatings there is no direct correlation between the surface roughness and the number of coatings applied to the substrate. As the particle loading increases, there is a slight increase in surface roughness for both single and double layer coatings. Furthermore, greater variation in the surface roughness was observed as the particle loading increased.

4.4.2 IPA-ST Nanocomposites

IPA-ST silica nanocomposites were prepared in the same manner as the IPA-ST-L coatings with similar concentrations. Colloidal dispersion concentrations shown in Table 3.2 yielded nanocomposite coatings with 35.3 wt% (19.7 vol%), 59.5 wt% (39.7 vol%) and 68.9 wt% (50 vol%) silica nanocomposite films for each respective increasing concentration of particles. All films were transparent and uniform. During AFM measurements the sample position was randomly oriented to eliminate any bias in the surface measurements. Figure 4.8 shows the three dimensional images for the IPA-ST nanocomposites for single and double layer films. A, C, E are single layer coatings; B, D, F are double layer coatings. All scans were performed with a 10μm x 10μm scan size. Table 4.4 shows the delta z-height and R_q values for each image in Figure 4.8.

Using such small particles posed a very difficult challenge to distinguish the surface topology between not only the concentrations of the particles in the films but also between single film coatings and double coatings. Moreover, when obtaining 'perfect' images, all data appeared and looked to be the same. Therefore, imperfections were found to clearly identify and distinguish between sample sets. One of the most beneficial factors about the Gwyddion software program is the ability of the mask function to be applied to either include, exclude, or separately use a given area designated by the user in the image for analysis. Therefore, the effect of any imperfections on the resulting data can be seen and determined if the data can be used in a valid manner.

Figure 4.8 A) shows what appears to be a canyon imperfection in the lower right corner of the topography scan. Figure 4.9 shows the same image but with the view from the z-axis. In Figure 4.9 the canyon appears to be a crack within the nanocomposite coating. The curing of the particular sample was cracked likely due to improper coating of the colloidal dispersion, drying time, curing time, or all of the previously mentioned. A simple mask was implemented within Gwyddion and the data was extracted. Figure 4.8 B) also shows the presence of dust or a non-coating type material on the surface of the nanocomposite. Again here a rectangular mask was chosen to block out that portion of the image when calculating the surface roughness. Figure 4.9 also shows the vertical topographic image of Figure 4.8 B with the mask applied.

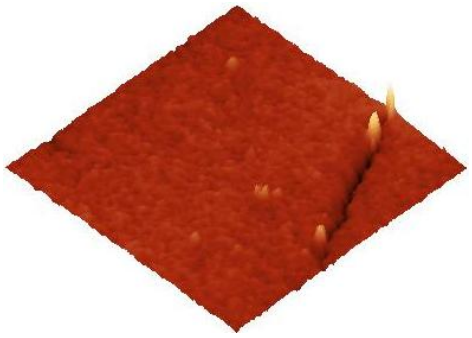

A) 20 vol % 1 Layer

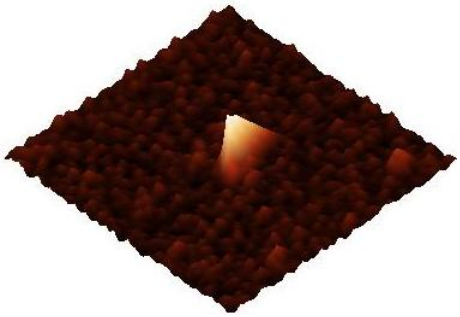

B) 20 vol % 2 Layers

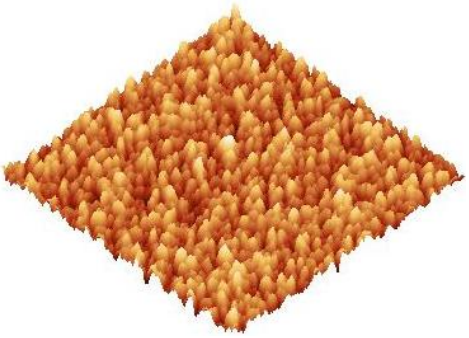

C) 40vol % 1 Layer

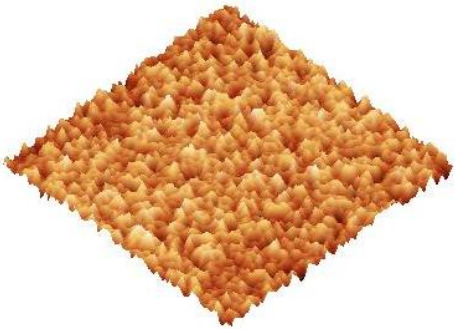

D) 40vol % 2 Layers

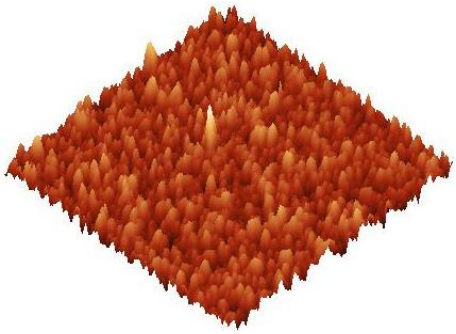

E) 50 vol % 1 Layer

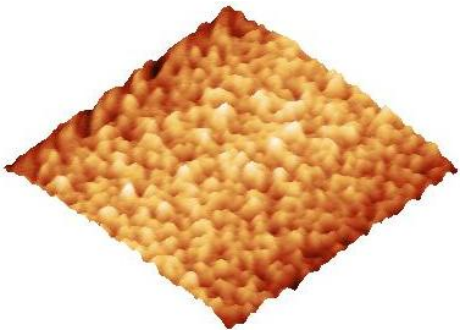

F) 50 vol % 2 Layers

Figure 4.8 Shows the 3-D scans for the respective volume concentrations of IPA-ST silica nanoparticle nanocomposites. A, C, E are single layer coatings; B, D, F are double layer coatings. All scans were performed with a 10 μm x 10 μm scan size.

Table 4.4 Shows the surface roughness values and the height differential values for each respective figure in Figure 4.8.

Figure	Δ Z height [μm]	R_q [nm]
A	0.098	3.7
B	0.250	9.7
C	0.075	9.7
D	0.043	6.1
E	0.083	8.1
F	0.075	9.5

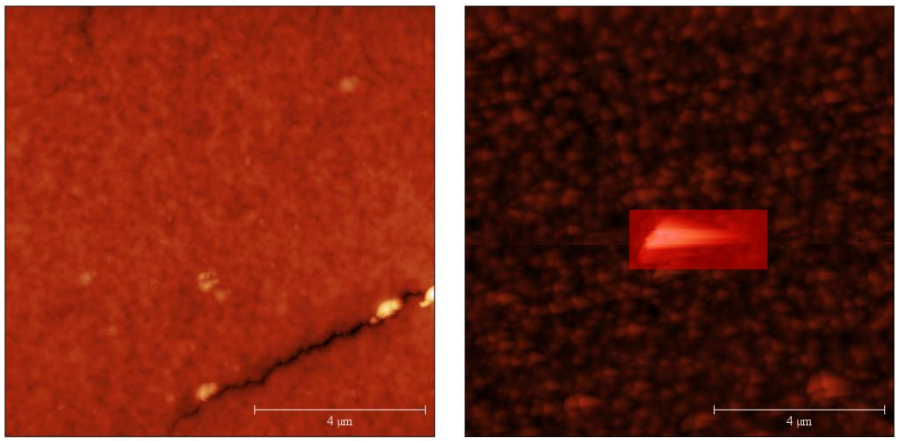

Figure 4.9 Shows the vertical image of Figure 4.8 A (left) and B (right) – the 20 vol % IPA-ST colloidal silica nanocomposite coatings, both single and double layers.

Figure 4.10 shows the averaged roughness, R_q, for the IPA-ST nanocomposite films. The 20 vol. % sample produced an average R_q = 3.71 nm (σ = 0.75 nm) and R_q = 9.52 nm (σ = 1.27 nm) for single and double layer nanocomposites, respectively. The 40 vol. % sample produced an average R_q = 9.94 nm (σ = 0.32 nm) and R_q = 6.04 nm (σ = 0.76 nm) for single and double layer nanocomposites, respectively. The 50 vol. % sample produced an average R_q = 7.98 nm (σ = 0.16 nm) and R_q = 8.45 nm (σ = 1.45 nm) for single and double layer nanocomposites, respectively. The error bars indicate the grand mean standard deviation. Furthermore, the red error bars represent the double layer film coating at 50 vol. % loading. The single layer coating at 50 vol % showed very little variation in the coating measurements.

For single layer coatings, the surface roughness increased as the concentration of silica nanoparticles increased. As the concentration of silica increased in the single layer coatings the surface roughness increased. The surface roughness for the 40 vol. % loading was higher than the 50 vol. % loading. The double layer coatings for the smallest and largest particle loading exhibited a higher surface roughness than single layer coatings. However, the 40 vol. % had a lower surface roughness than the single layer coating. Table 4.4 shows that the delta-z height decreased for all double layer coatings except for the 20 vol. % loading. The increase in delta-z was a direct result of the large 'mountain' peak which was uncharacteristic of the remainder of the film coating. The surface roughness for these samples appears to be independent of the sample height change. For this system, R_q for single layer coatings increased as the particle loading increased. As the concentration of IPA-ST particles increased the variation in the surface roughness also decreased for single layer coatings.

The decrease in surface roughness for the 40 vol. % loading for the double layer coating was also present in the IPA-ST-L samples. Both the IPA-ST (~13.65 nm particles) and IPA-ST-L (~46.8 nm particles) showed a decrease in surface roughness for the double-layer coatings compared to single layer coatings at 40 vol % particle loading. According to Table 4.4 and Figure 4.10 there is no correlation between the R_q values and the number of coatings applied to a substrate. The surface roughness values for IPA-ST coatings were less than the surface roughness values for IPA-ST-L coatings. The smaller particles produced a smoother surface, regardless of particle loading. The average R_q for

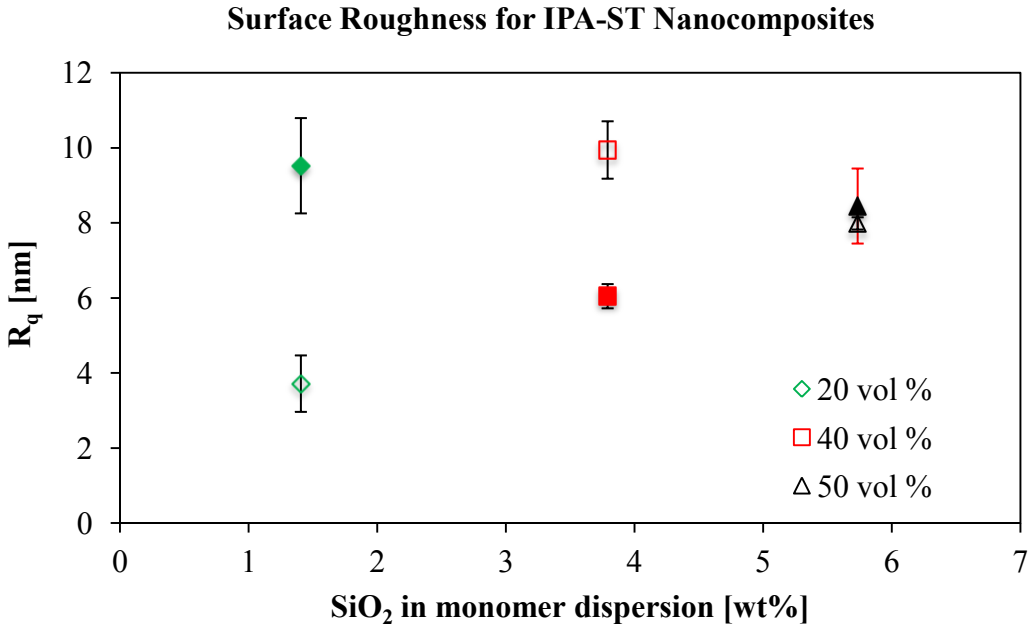

Figure 4.10 Average surface roughness for single and double layer IPA-ST nanocomposite coatings. Open symbols are single layer films. Closed symbols are double layer films. The volume percentage of silica in the solid films is also indicated.

the 20 vol % particle loading single coating was very close to R_q for the neat polymer coating. Changes in R_q for IPA-ST particles become noticeably present once higher concentration particles are used or multiple layers are applied to the substrate.

One of the common defects observed in samples is shown in Figure 4.11. Figure 4.11 shows the z-axis top down view of Figure 4.8 F. This particular sample shows striations which can arise during the spin coating procedure. Striations will occur when the spin exhaust rate, spin acceleration, or spin speed is too high, and can also occur when fluid is deposited off center of the coated substrate. The sample in Figure 4.11 had striations due to the fluid being deposited off center. Almost all samples, exhibit some type of streaking towards the boundary limits. However, the area of interest remains the uniform coatings and boundary limits were not examined.

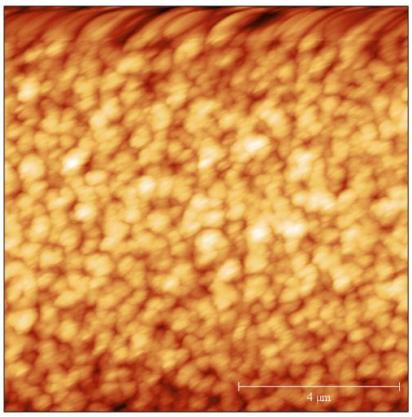

Figure 4.11 Shows the top down view on the z-axis of Figure 4.8 F with striations along the top portion of the image.

4.4.3 IPA-ST-ZL Nanocomposites

IPA-ST-ZL silica nanocomposites were prepared using the methods previously described. Colloidal dispersion concentrations shown in Table 3.2 yielded nanocomposite coatings with 35.6 wt% (19.9 vol. %), 60.04 wt% (40.32 vol. %) and 69.7 wt% (50.8 vol. %) silica nanocomposite films for each respective increasing concentration of particles. All films were transparent and uniform. During AFM measurements the sample position was randomly oriented to eliminate any bias in the surface measurements. Figure 4.12 shows the three dimensional images for the IPA-ST nanocomposites for single and double layer films. A, C, E are single layer coatings; B, D, F are double layer coatings. All scans were performed with a 10 μm x 10 μm scan size. Table 4.5 shows the delta z-height and R_q for each image in Figure 4.12.

The largest size particles used to analyze the surface roughness of ultra-thin film nanocomposites showed the largest surface roughness values out of all samples. The topology images A-F of ST-ZL nanocomposites in Figure 4.13 are visually the easiest to distinguish between the particle loading when compared to ST and ST-L samples. Unlike IPA-ST and ST-L coatings the variation in R_q for IPA-ST-ZL coatings did not change as drastically. Figure 4.14 demonstrates this as shown by the error bars which represent ± the grand mean standard deviation. The red error bars represent the double layer film coatings at 20 and 50 vol. % nanoparticles. Table 4.5 also shows that samples with a higher delta-z height have a higher surface roughness. Similarly to ST and ST-L coatings it is difficult to establish any correlation between the R_q values and delta-z height.

Figure 4.14 shows the averaged roughness, R_q, for the IPA-ST nanocomposite films. The 20 vol. % sample produced an average R_q = 27.6 nm (σ = 0.85 nm) and R_q = 27.2 nm (σ = 2.57 nm) for single and double layer nanocomposites, respectively. The 40 vol. % sample produced an average R_q = 24.3 nm (σ = 0.72 nm) and R_q = 35.1 nm (σ = 2.36 nm) for single and double layer nanocomposites, respectively. The 50 vol. % sample produced an average R_q = 23 nm (σ = 1.21 nm) and R_q = 23.36 nm (σ = 1.76 nm) for single and double layer nanocomposites, respectively.

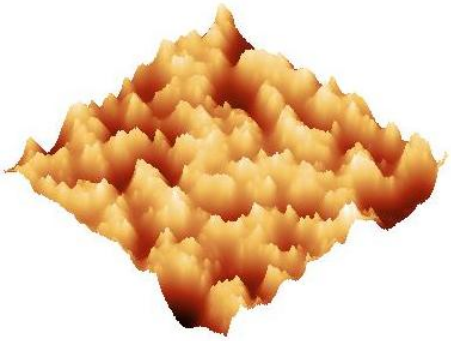

A) 20 vol % 1 Layer

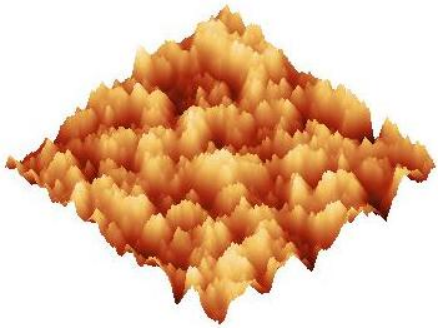

B) 20 vol % 2 Layers

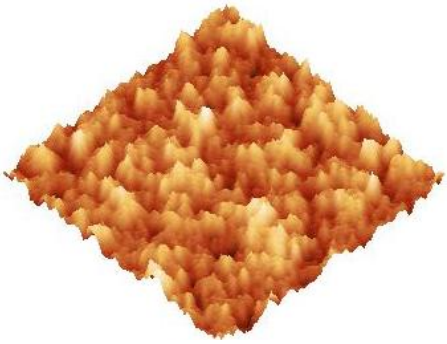

C) 40 vol % 1 Layer

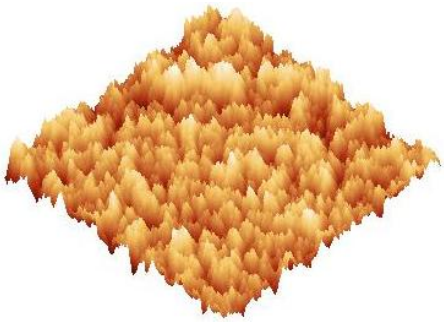

D) 40 vol % 2 Layers

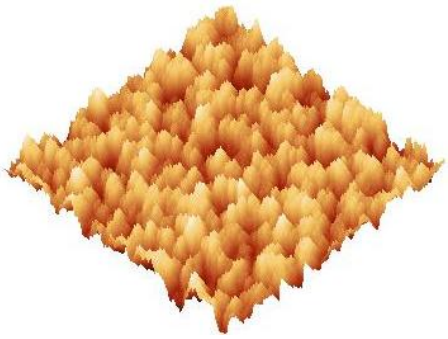

E) 50 vol % 1 Layer

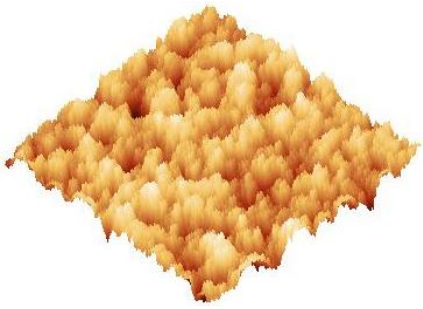

F) 50 vol % 2 Layers

Figure 4.12 Shows the 3-D scans for the respective volume concentrations of IPA-ST-ZL silica nanoparticle nanocomposites. A, C, E are single layer coatings; B, D, F are double layer coatings. All scans were performed with a 10 μm x 10 μm scan size.

Table 4.5 Shows the surface roughness values and the height differential values for each respective figure in Figure 4.8.

Figure	Δ Z height [μm]	R_q [nm]
A	0.24	28.0
B	0.19	27.6
C	0.21	23.5
D	0.28	32.7
E	0.17	23.8
F	0.21	27.0

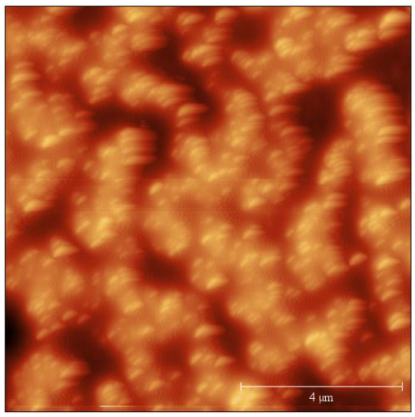

A) 20 vol % 1 Layer

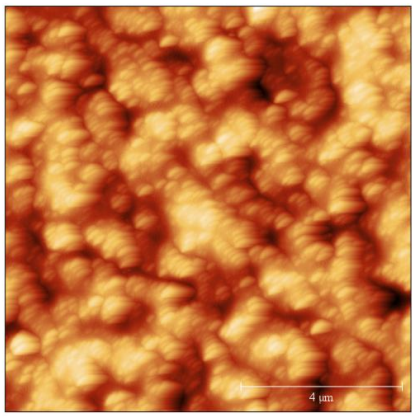

B) 20 vol % 2 Layers

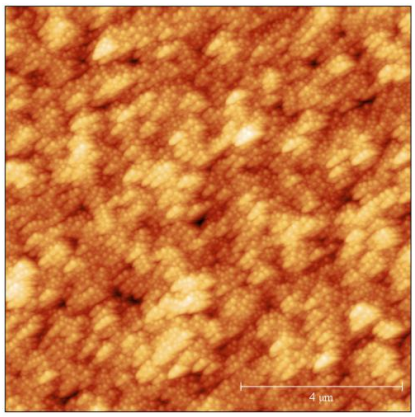

C) 40 vol % 1 Layer

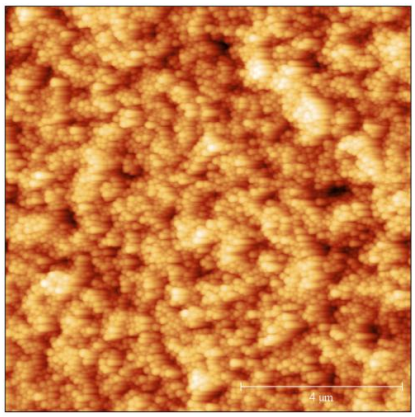

D) 40 vol % 2 Layers

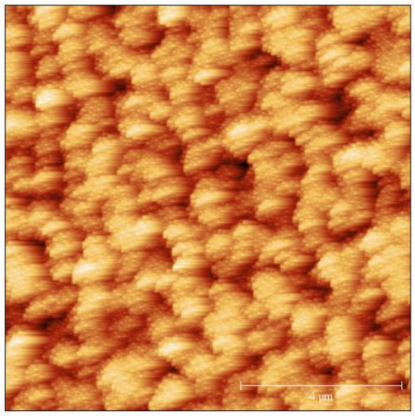

E) 50 vol % 1 Layer

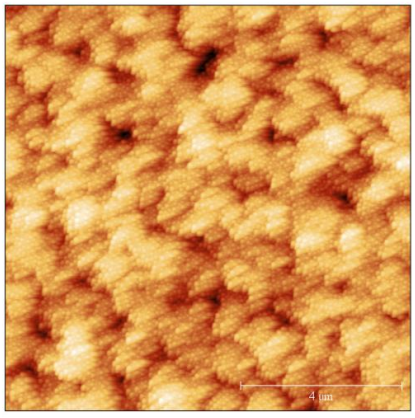

F) 50 vol % 2 Layers

Figure 4.13 Shows the top down view from the z-axis of Figure 4.12 for each respective nanocomposite coating.

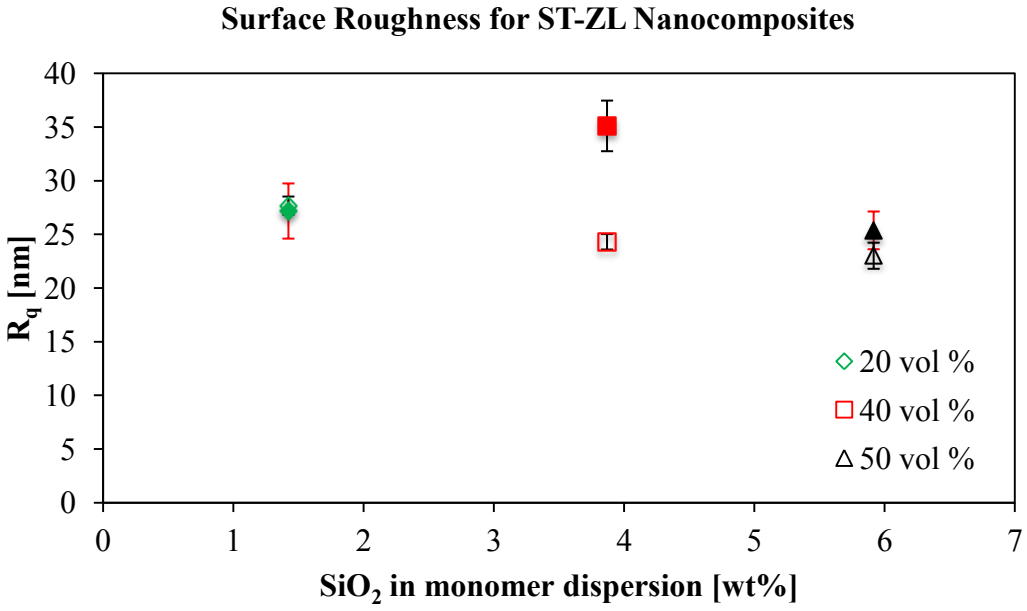

Figure 4.14 Average surface roughness for single and double layer IPA-ST-ZL nanocomposite coatings. Open symbols are single layer films. Closed symbols are double layer films. The volume percentage of silica in the solid films is also indicated.

The surface roughness values for single layer ZL nanocomposites decreases slightly as the concentration of particles increases from 20 to 50 vol. % loading. Figure 4.14 shows the surface roughness decrease slightly as the concentration decreases for single layer nanocomposite coatings. The surface roughness values for double layer ZL nanocomposites also decreases slightly as the concentration of particles increases from 20 to 50 vol. % loading. However, the 40 vol. % loading of the double layer nanocomposite had the highest average surface roughness value out of any sample. Similarly to the ST, and ST-L particles, the 40 vol. % loading of particles exhibit unexplainable surface roughness values when comparing to the smallest and largest particle loadings.

4.4.4 Peak Height Distributions

The one-dimensional peak height distributions for all samples were checked to determine if deconvolution of ST, ST-L, and ST-ZL nanocomposites was necessary. Deconvolution simply reveals data hidden by both signal-to-noise ratios or peaks hidden due to the limitations of the scanning procedure used on AFM. Figure 4.15 shows the peak height distributions for neat, ST, ST-L, and ST-ZL particles. All distributions were normally distributed. As the particle size increased, the peak height distributions for each nanocomposite coating broadened and the peak height increased as well. This supports the data representing the effect of particle size on surface roughness.

Previous studies performed by Kanniah [1] consisted of ultra-thin film nanoparticles with varying size particles. Using varying size nanoparticles (10 nm and 100 nm) with mixed ratios of the small and large particles in the nanocomposite coating required deconvolution in order to correct for the height distributions for mixed size nanocomposites. In this particular study, the same size nanoparticles were used for coatings for all samples. Since the particle size distributions were unimodal, and monodispersed, and the peak height distributions were normal - deconvolution of the data was not necessary. Peak height distributions did not vary between the number of coatings applied on the nanocomposite.

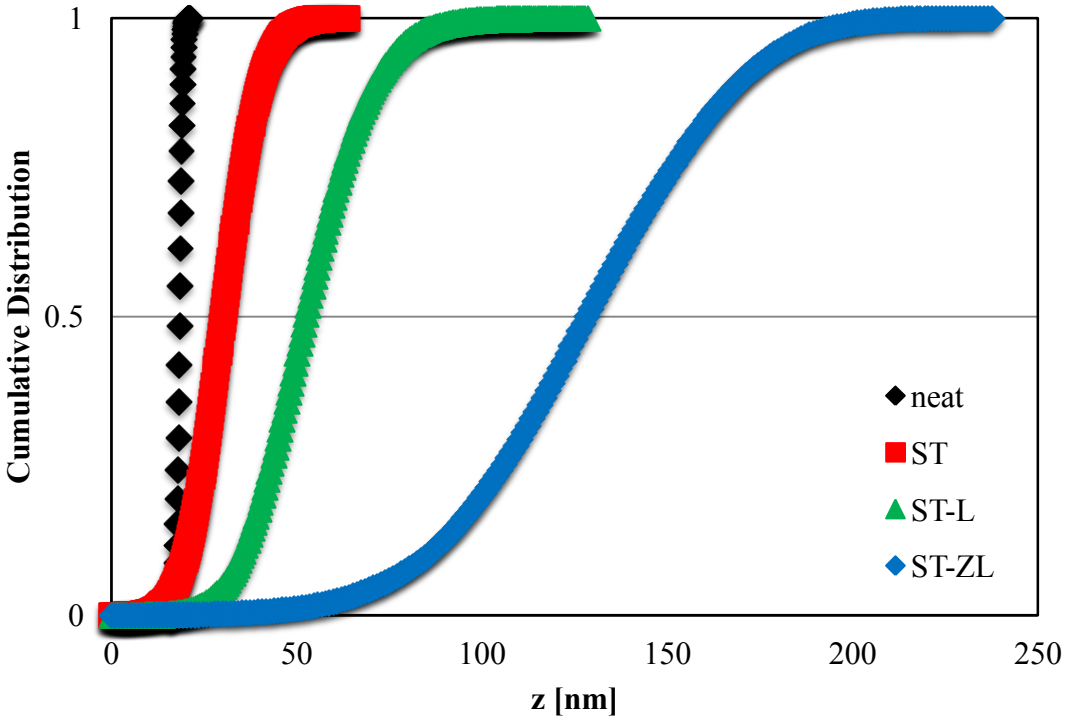

Figure 4.15 Shows the cumulative peak height distributions for thin film nanocomposites as a function of particle size.

4.5 Particle size and surface roughness

The surface roughness was also determined as a function of particle size. Figure 4.16 shows the average surface roughness for 20 volume percent loading in the nanocomposite films for all three types of nanoparticles. Both the single and double layer surface roughness values increase in a linear fashion as the particle size increases. Small concentrations of IPA-ST particles (~13 nm) in the single coating layer show almost no change in the surface roughness when compared to a neat polymer coating. However, after application of a second thin film coating, the surface roughness increased more than expected. Increasing the particle size at 20 vol% does show an overall increase in the surface roughness. There was almost no difference when comparing the surface roughness of single or double layer coatings for the ST-L and ST-ZL coatings.

Figure 4.17 shows the average surface roughness for 40 volume percent loading in the nanocomposite films for all three types of nanoparticles. Single and double layer nanocomposites increase in surface roughness linearly as the particle size increases. Both ST and ST-L nanocomposites produced single layer coatings which had a greater surface roughness than the double layer coating. The surface roughness of the double-layer coating was not expected to be lower than the single layer coating for ST and ST-L particles. The double-layer coating for ST-ZL surface roughness was significantly higher than the single layer coating. The average roughness was the highest out of any recorded surface roughness measurement and was expected to be lower. Similarly, to Figure 4.16, the surface roughness increased in a linear fashion with the increase in particle size.

Figure 4.18 shows the average surface roughness for 50 volume percent loading in the nanocomposite films for all three sizes of nanoparticles. Single and double layer nanocomposites increase in surface roughness in a logarithmic trend. This surface roughness for ST-L particles was slightly higher at 50 vol. % loading than the lower concentrations. The surface roughness is highly dictated by the particle size and not the particle volume loading.

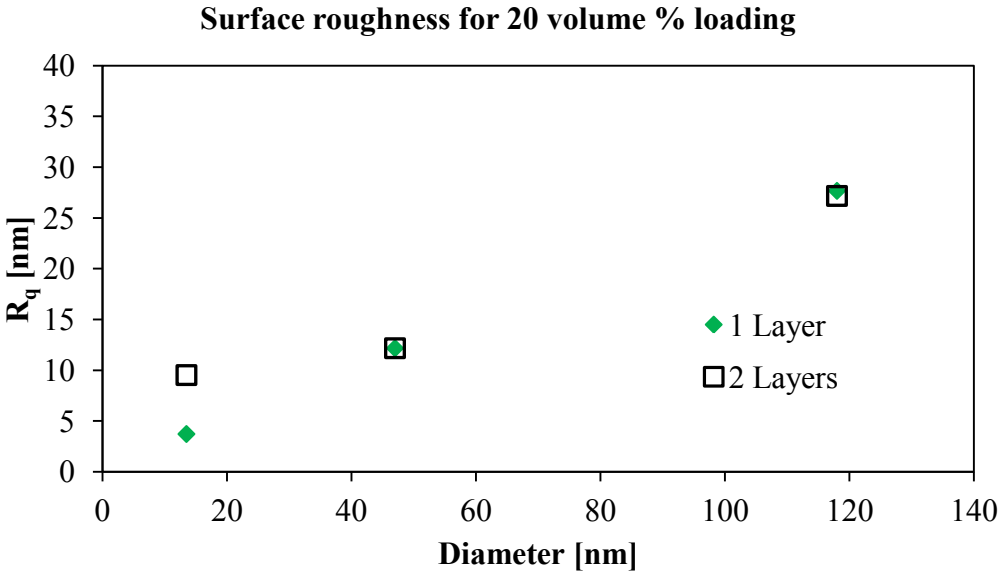

Figure 4.16 Average surface roughness for 20 volume percent loading in the nanocomposite films for all three types of nanoparticles.

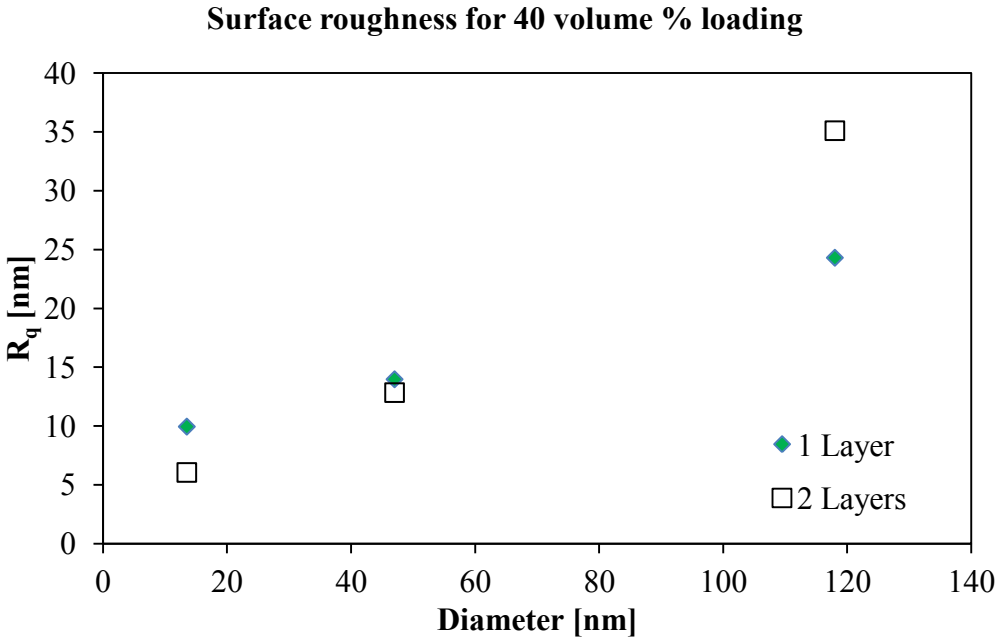

Figure 4.17 Average surface roughness for 40 volume percent loading in the nanocomposite films for all three types of nanoparticles

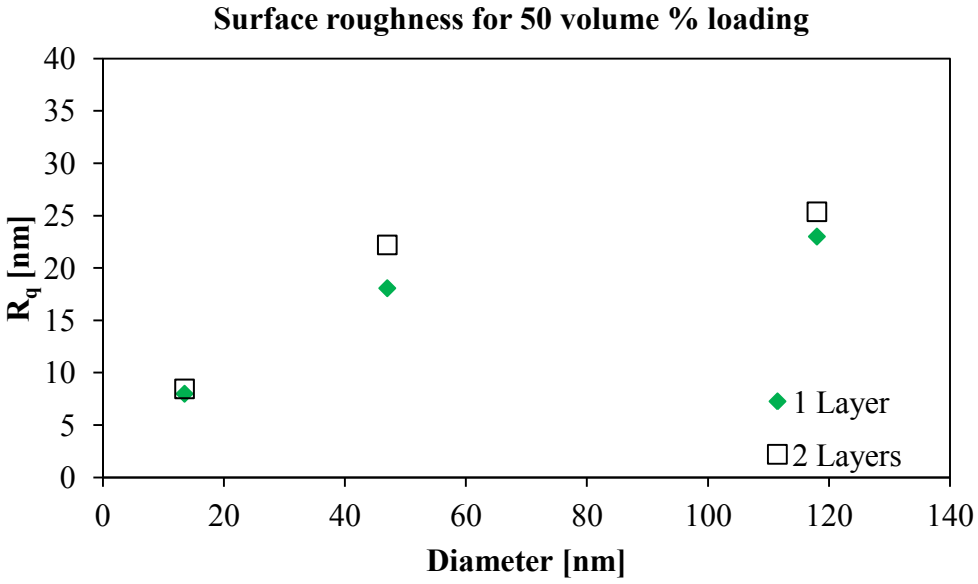

Figure 4.18 Average surface roughness for 50 volume percent loading in the nanocomposite films for all three types of nanoparticles

Figure 4.19 shows the estimation of the surface roughness using the delta-z height change obtained from AFM. The two blue points represent the IPA-ST single (Δ z = 100) and double (Δ z = 250) layer coating samples at 20 vol. % particle loading. Using linear regression, for the entire data set, $R^2 = 0.630$. Excluding the two IPA-ST samples at 20 vol. % increases the R^2 to 0.867 for the regression fitting. The surface roughness for all samples was on average 12% of the delta-z value measured.

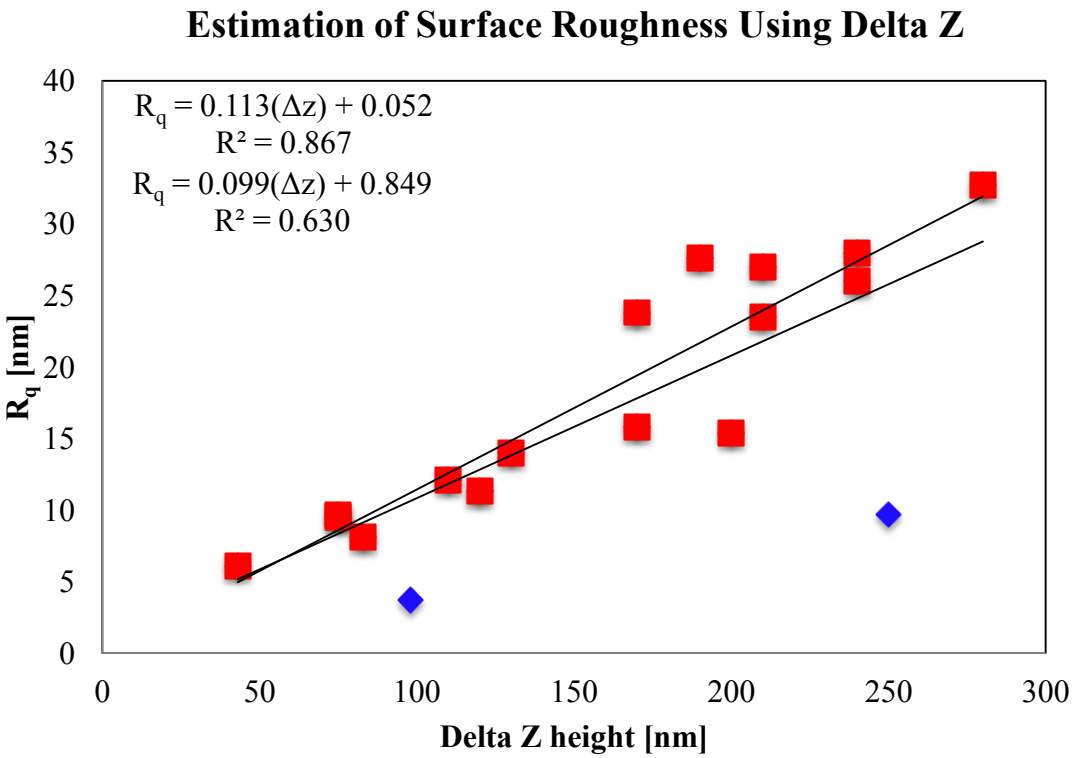

Figure 4.19 Estimation of the surface roughness based on the delta-z height obtained using AFM.

Chapter 5 Conclusions

5.1 Summary

Developing ultrathin film nanocomposites can be challenging when trying to address multiple performance properties. For optical applications, properties such as the haze or refractive index are often examined. These properties could easily be affected by the particle size or loading, especially on the nanoscale. The surface chemistry of the nanoparticle filler and volume fraction in the nanocomposite can affect the performance properties of the ultrathin film. This work compared the effect particle size and loading had on the surface roughness of ultrathin film nanocomposites. An acrylate based monomer was used as the continuous phase and monodispersed silica nanoparticles were used as the discontinuous phase.

The particle size distribution of colloidal dispersions can be measured multiple ways. Dynamic light scattering and transmission electron microscopy were used to determine the particle size of three different sizes of industrially synthesized silica particle dispersions. TEM provides researchers with a primary particle size while DLS shows the hydrodynamic particle size. If agglomeration of the particles is present, larger particle size distributions or multi-model particle size distributions will most likely occur using DLS. TEM is the preferred method for determining the primary particle size of dilute colloidal dispersions, but data analysis is more time consuming.

Ultra-thin film nanocomposites with three different size silica nanoparticles were prepared. The effect of the concentration of nanoparticles and size of the particles incorporated into a polymer matrix was examined. Samples showed a wide range of results depending on the particle size. IPA-ST (~13 nm particles) coatings showed the greatest variance between surface roughness measurements. IPA-ST-ZL (~120 nm) coatings showed the least variance between surface roughness measurements. Typical film thickness of single layer coatings ranged from 120 to 170 nm, and two layer coatings ranged from 300 to 450 nm. No correlation between surface roughness and the number of layers applied to the substrate was found. The surface roughness of silica-acrylate nanocomposites varied more based on the particle size rather than particle loading for any

size particles used. The surface roughness of the ultrathin films ranged from R_q = 3-11, R_q = 11-26, and R_q = 21-37 for nominal diameters 13, 45, and 120 nm, respectively. Changing the particle loading would increase surface roughness a maximum of 167%, 72%, 29% for ST, ST-L, and ST-ZL nanoparticles, respectively. Furthermore, changing the particle loading would sometimes decrease the surface roughness a maximum of 36%, 34%, and 27% for ST, ST-L, and ST-ZL nanoparticles, respectively. The surface roughness also would increase on average 10-15% with the addition of a second ultrathin nanocomposite coating. However, increasing the particle size always showed an increase in surface roughness for a given particle loading. The surface roughness increased a maximum of 644%, 480%, and 200% as the particle size increased for 20, 40, and 50 volume percent loading, respectively. The surface roughness measured approximately 12% of the delta-z (which is defined as the difference between the maximum peak and minimum peak of the AFM scan) peak height measured on AFM.

The unique behavior of the surface roughness for all samples at 40 vol. % loading was independent of particle size and most likely due to improper method of preparing the samples. Aggregation of the particles might occur more at 40 vol. % loading than other concentrations as the solvent system evaporates leaving a sol-gel type material before curing. Particle loading had a larger effect on the surface roughness for IPA-ST coatings than any other samples.

The largest contributing factor to altering the surface roughness is the size of the nanoparticles incorporated into the particle matrix. Larger particles will produce a surface with a higher surface roughness. The surface roughness cannot be determined thus far to have any correlation with the number of layers of ultra-thin film nanocomposite applied to a given substrate. Controlling the surface roughness provides researchers with the ability to produce coating materials with either superhydrophobic or superhydrophilic properties, change the layer-by-layer adhesion, or layer-substrate adhesion. By changing the size and concentration of the nanoparticles the adsorption or reflectance of light is also altered. This allows researchers to possibly make ultra-thin film nanocomposites which are highly specific optical filters.

5.2 Future Work

Other properties such as the haze and refractive index should be measured for all types of samples to determine if any relationship exists. A more comprehensive study with varying concentrations and layers of nanocomposite would be needed to definitively determine a correlation, if any exist, with the surface roughness and the number of layers applied. Furthermore, more data would need to be collected to determine a better correlation between the delta-z values and surface roughness for concentrations other than reported. Determination if the relationships discovered with unimodal particle size distributions can be applied to bimodal particle size distributions would also be pertinent. The use of mixed size bimodal nanoparticles can provide researchers with the ability to even further tailor the surface roughness to a specific value.

Although precise control of the coating method was maintained, difficulty would arise if these coating are transferred to other types of surfaces – either curved surfaces or surfaces larger in diameter. Investigation of the surface roughness would also be interesting if more than two layers of nanocomposites are applied to a substrate. The surface roughness should be determined by the governing surface coating – but might exhibit more bulk phase behavior.

Nomenclature

Chapter 2

$I(t)$	random function of time
Γ	time decay constant
t	time
q	magnitude of the scattering vector
θ	scattering angle
n	index of refraction of the solution
λ	laser wavelength
D	translational diffusion coefficient of solute
k	Boltzmann's constant
T	the absolute temperature
η	viscosity
R_h	hydrodynamic radius
$G_I[d]$	intensity-weighted differential particle size distribution
$G_V[d]$	volume-weighted differential particle size distribution
$G_N[d]$	number-weighted differential particle size distribution
C[d]	cumulative particle size distribution
M	light scattering coefficient, M=1 for d < 25 nm

Chapter 4

R_q	root mean square roughness
N	sample size
z_j	height of each data point collected
$\bar{z}$	average height of all data points collected
d(H)	hydrodynamic diameter
D	translational diffusion coefficient

k	Boltzmann’s constant
T	absolute temperature
η	viscosity

Appendix A

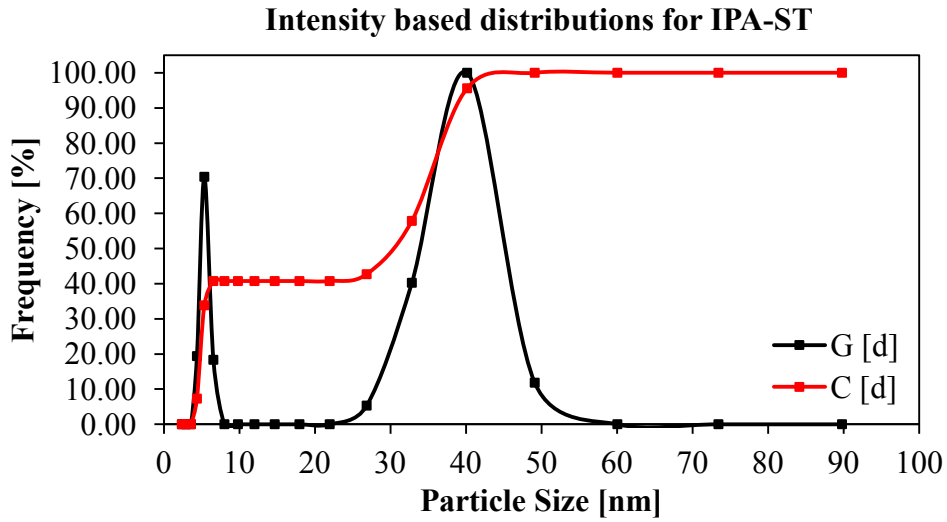

Intensity-weighted differential and cumulative frequency distribution functions for IPA-ST colloidal silica dispersion suspension of silica nanoparticles. Concentration was less than 0.1 wt% silica.

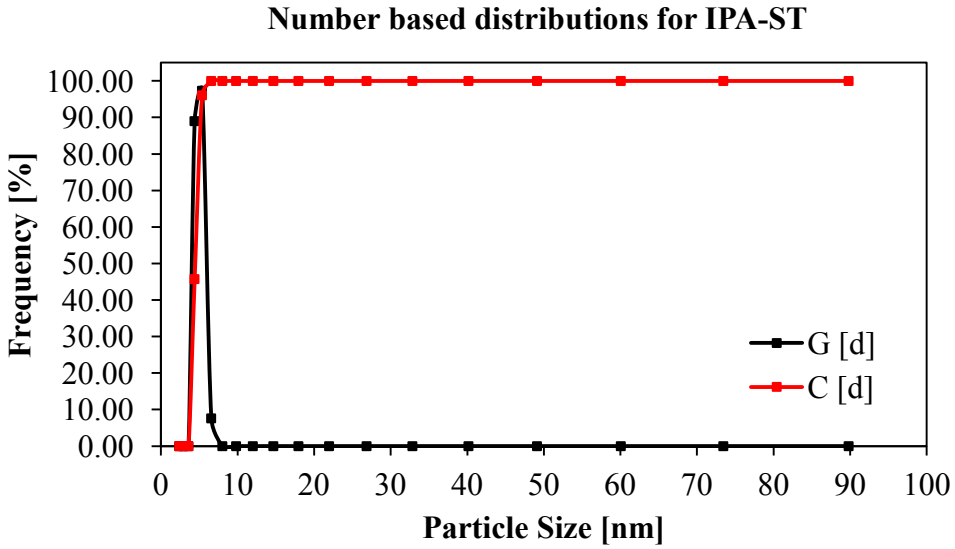

Number-weighted differential and cumulative frequency distribution functions for IPA-ST colloidal silica dispersion suspension of silica nanoparticles. Concentration was less than 0.1 wt% silica.

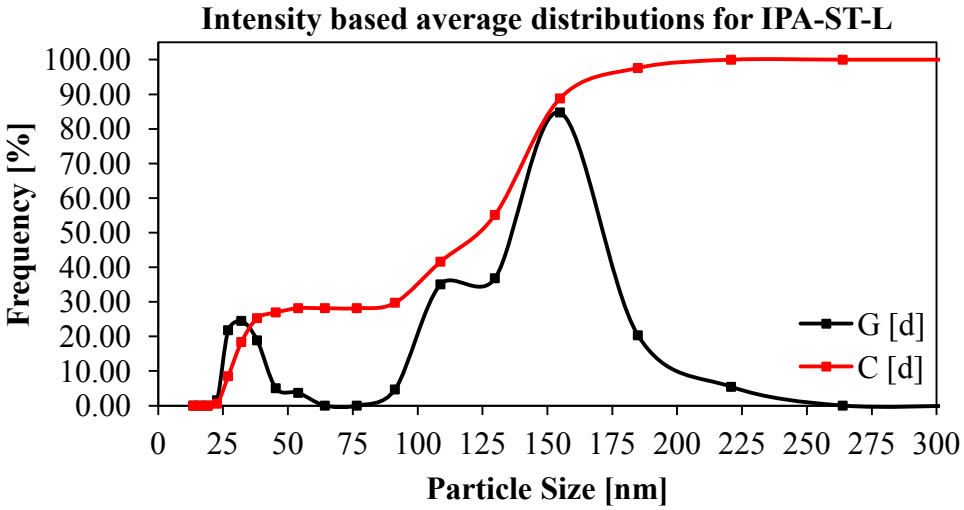

Intensity-weighted differential and cumulative frequency distribution functions for IPA-ST-L colloidal silica dispersion suspension of silica nanoparticles. Concentration was less than 0.1 wt % silica.

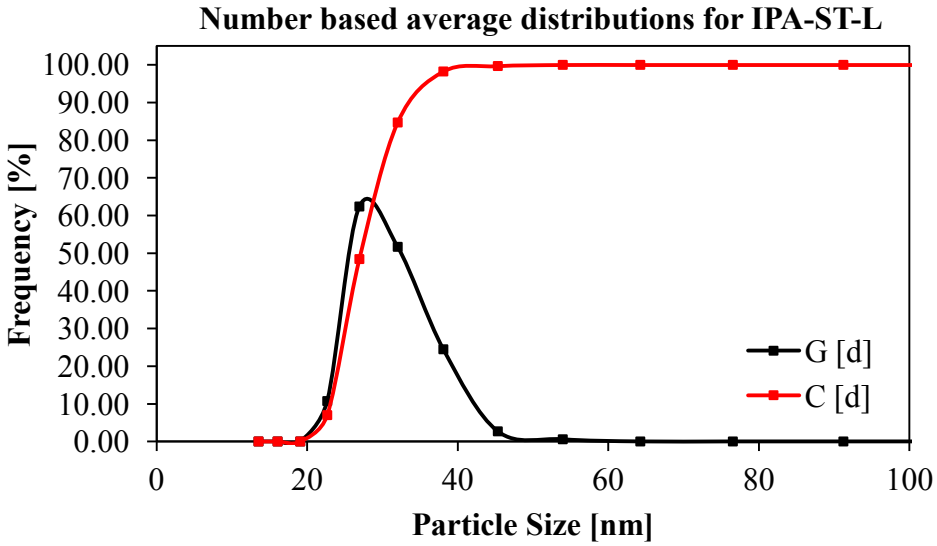

Number-weighted differential and cumulative frequency distribution functions for IPA-ST-L colloidal silica dispersion suspension of silica nanoparticles. Concentration was less than 0.1 wt% silica.

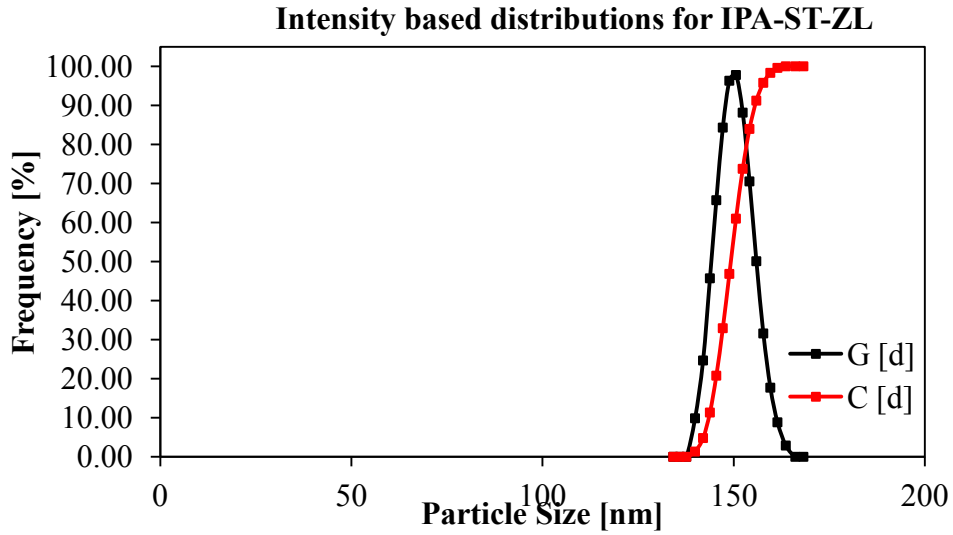

Intensity-weighted differential and cumulative frequency distribution functions for IPA-ST-ZL colloidal silica dispersion suspension of silica nanoparticles. Concentration was less than 0.1 wt % silica.

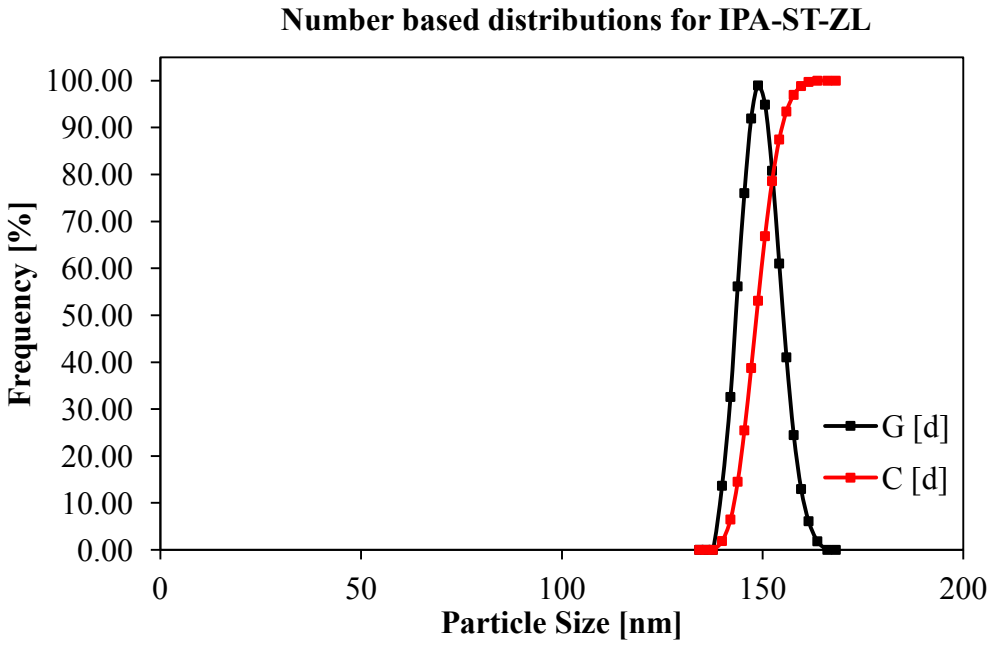

Number-weighted differential and cumulative frequency distribution functions for IPA-ST-ZL colloidal silica dispersion suspension of silica nanoparticles. Concentration was less than 0.1 wt% silica.

Appendix B

1.41 wt % SiO_2 , Single Layer ($\alpha = 0.05$)			
µm vs. µm	P-value	F	F crit
5 vs. 10	0.527	0.479	7.7086
5 vs. 25	0.396	0.9	7.7086
10 vs. 25	0.580	0.36	7.7086
1.41 wt % SiO_2 , Double Layer ($\alpha = 0.05$)			
µm vs. µm	P-value	F	F crit
5 vs. 10	0.007	25.17	7.7086
5 vs. 25	0.281	1.547	7.7086
10 vs. 25	0.057	7.034	7.0786

3.91 wt % SiO_2 , Single Layer ($\alpha = 0.05$)			
µm vs. µm	P-value	F	F crit
5 vs. 10	0.883	0.024	7.7086
5 vs. 25	0.627	0.276	7.7086
10 vs. 25	0.544	0.438	7.7086
3.91 wt % SiO_2 , Double Layer ($\alpha = 0.05$)			
µm vs. µm	P-value	F	F crit
5 vs. 10	0.910	0.014	7.7086
5 vs. 25	0.075	5.67	7.7086
10 vs. 25	0.065	6.312	7.0786

5.99 wt % SiO_2 , Single Layer ($\alpha = 0.05$)			
µm vs. µm	P-value	F	F crit
5 vs. 10	0.256	1.755	7.7086
5 vs. 25	0.022	13.39	7.7086
10 vs. 25	0.204	2.299	7.7086
5.99 wt % SiO_2 , Double Layer ($\alpha = 0.05$)			
µm vs. µm	P-value	F	F crit
5 vs. 10	0.082	5.33	7.7086
5 vs. 25	0.161	2.941	7.7086
10 vs. 25	0.328	1.237	7.0786

References

1. Kanniah, V., *Nanoparticle Additives For Multiphase Systems: Synthesis, Formulation and Characterization*, in *Chemical Engineering*2012, University of Kentucky: Lexington KY.
2. Lainovic, T., et al., *Determination of surface roughness and topography of dental resin-based nanocomposites using AFM analysis.* Bosnian J. Basic Med. Sci., 2013. **13**(1): p. 34-43.
3. Yamada, S., E. Mouri, and K. Yoshinaga, *Incorporation of titanium dioxide particles into polymer matrix using block copolymer micelles for fabrication of high refractive and transparent organic-inorganic hybrid materials.* J. Polym. Sci., Part A Polym. Chem., 2011. **49**(3): p. 712-718.
4. Althues, H., J. Henle, and S. Kaskel, *Functional inorganic nanofillers for transparent polymers.* Chem. Soc. Rev., 2007. **36**(9): p. 1454-1465.
5. Hall, D.B., P. Underhill, and J.M. Torkelson, *Spin coating of thin and ultrathin polymer films.* Polym. Eng. Sci., 1998. **38**(12): p. 2039-2045.
6. Minelli, C., et al., *The influence of nanoparticle fillers on the morphology of a spin-cast thin film polymer blend.* Colloid Polym. Sci., 2006. **284**(5): p. 482-488.
7. Ghosh, S.S., et al., *Why specific mixed solvent composition leads to appropriate film formation of composite during spin coating?* Appl. Phys. Lett., 2013. **102**(5): p. 051918/1-051918/5.
8. Sharma, P.R.S. and H.L. Frisch, *Urethane containing interpenetrating polymer networks (IPN's) for nonlinear optical (NLO) properties.* 60 Years Polyurethanes, [Int. Symp. Exhib.], 1998: p. 186-203.
9. Zhou, T.H., et al., *A novel route for improving creep resistance of polymers using nanoparticles.* Compos. Sci. Technol., 2007. **67**(11-12): p. 2297-2302.
10. Zhou, T.H., et al., *In-situ crosslinking induced structure development and mechanical properties of nano-silica/polypropylene composites.* Key Eng. Mater., 2007. **334-335**(Pt. 2, Advances in Composite Materials and Structures): p. 733-736.
11. Coutinho, C.A., D. Walker, and V.K. Gupta, *Synthesis and characterization of interpenetrating networks functionalized with nanoparticles of titanium dioxide.* Abstracts, 58th Southeast Regional Meeting of the American Chemical Society, Augusta, GA, United States, November 1-4, 2006: p. SRM06-150.
12. Sugimoto, H., et al., *Preparation and properties of urethane acrylate-epoxy interpenetrating polymer networks containing silica nanoparticles.* Polym. Bull. (Heidelberg, Ger.), 2006. **57**(6): p. 975-982.
13. Risse, G. and M. Koch, *Non-adhesive protective layer from crosslinked nanoparticles for printing rolls*, 2006, (Koenig & Bauer A.-G., Germany). p. 8 pp.
14. Tang, D., et al., *Influence of BaTiO3 on damping and dielectric properties of filled polyurethane/unsaturated polyester resin interpenetrating polymer networks.* J. Mater. Sci., 2005. **40**(13): p. 3339-3345.
15. Kausch, H.H. and M. Dettenmaier, *On some mechanical effects in glassy polymers attributed to chain entanglements.* Colloid Polym. Sci., 1982. **260**(2): p. 120-3.

16. Carrion, F.J., J. Sanes, and M.-D. Bermudez, *Influence of ZnO nanoparticle filler on the properties and wear resistance of polycarbonate.* Wear, 2007. **262**(11-12): p. 1504-1510.
17. Godovsky, D.Y., *Device applications of polymer-nanocomposites.* Adv. Polym. Sci., 2000. **153**(Biopolymers, PVA Hydrogels Anionic Polymerisation Nanocomposites): p. 163-205.
18. Arango, A.C., S.A. Carter, and P.J. Brock, *Charge transfer in photovoltaics consisting of interpenetrating networks of conjugated polymer and TiO2 nanoparticles.* Appl. Phys. Lett., 1999. **74**(12): p. 1698-1700.
19. Kim, P., et al., *Surface modification of barium titanate nanoparticles for dielectric nanocomposites.* PMSE Prepr., 2006. **94**: p. 10-11.
20. Smith, G.B., et al., *Nanoparticle-doped Polymer Foils for Use in Solar Control Glazing.* J. Nanopart. Res., 2002. **4**(1/2): p. 157-165.
21. Laskar, J., et al., *Synthesis and characterization of interpenetrating networks from polycarbonate and cellulose acetate butyrate.* Polymer, 2004. **45**(15): p. 5047-5055.
22. Sharma, P.R.S., P. Zhou, and H.L. Frisch, *Synthesis and characterization of interpenetrating polymer networks with nonlinear optical properties.* J. Polym. Sci., Part A: Polym. Chem., 1996. **34**(6): p. 1049-58.
23. Cho, E.J., et al., *Nanoparticle Characterization: State of the Art, Challenges, and Emerging Technologies.* Mol. Pharmaceutics, 2013. **10**(6): p. 2093-2110.
24. Anumolu, R. and L.F. Pease, III, *Rapid nanoparticle characterization.* Delivery Nanopart., 2012: p. 347-376.
25. Mandzy, N., E. Grulke, and T. Druffel, *Breakage of TiO2 agglomerates in electrostatically stabilized aqueous dispersions.* Powder Technol., 2005. **160**(2): p. 121-126.
26. Drzal, L.T., M.J. Rich, and P.F. Lloyd, *Adhesion of graphite fibers to epoxy matrices: I. The role of fiber surface treatment.* J. Adhes., 1983. **16**(1): p. 1-30.
27. Winey, K.I. and R.A. Vaia, *Polymer nanocomposites.* MRS Bull., 2007. **32**(4): p. 314-322.
28. Krishnamoorti, R., *Strategies for dispersing nanoparticles in polymers.* MRS Bull., 2007. **32**(4): p. 341-347.
29. Kaur, J., J.H. Lee, and M.L. Shofner, *Influence of polymer matrix crystallinity on nanocomposite morphology and properties.* Polymer, 2011. **52**(19): p. 4337-4344.
30. Rancourt, J.D., *Optical Thin Films: User Handbook*. 1996, Bellingham, Washington: SPIE-The International Society for Optical Engingeering.
31. Heilmeier, G.H., *Some Reflections on Innovation and Invention*, 1992: Founders Award Lecture, National Academy of Engineering, Washington, D.C.
32. Corporation, N.C.A. *Organosilicasol™*. 2007; Available from: http://www.nissanchem-usa.com/organosilicasol.php.
33. Phillies, G.D.J., *Quasielastic light scattering.* Anal. Chem., 1990. **62**(20): p. 1049A-1057A.
34. Goldburg, W.I., *Dynamic Light Scattering.* American Journal of Physics, 1999. **67**: p. 1152.
35. Siegert, A.J.F., *On the fluctuations in signals returned by many independently moving scatterers*. 1943, MIT Rad. Lab.: Massachusetts Institute of Technology.

36. Berne, B.J., Pecora, Robert, *Dynamic Light Scattering with Applications to Chemistry, Biology, and Physics*. 1976, New York: Wiley-Interscience.
37. Provencher, S.W., *CONTIN: A General Purpose Constrained Regularization Program for Inverting Noisy Linear Algebraic and Integral Equations.* Computer Physics Communications, 1982. **27**(3): p. 229-242.
38. Provencher, S.W., *A Constrained Regularization Method for Inverting Data Represented by Linear Algebraic or Integral Equations.* Computer Physics Communications, 1982. **27**(3): p. 213-227.
39. Bornside, D.E., C.W. Macosko, and L.E. Scriven, *Spin coating: one-dimensional model.* J. Appl. Phys., 1989. **66**(11): p. 5185-93.
40. Stange, T.G., et al., *Scanning tunneling microscopy and atomic force microscopy characterization of polystyrene spin-coated onto silicon surfaces.* Langmuir, 1992. **8**(3): p. 920-6.
41. Shafrin, E.G. and W.A. Zisman, *Constitutive relations in the wetting of low-energy surfaces and the theory of the retraction method of preparing monolayers.* Journal of Physical Chemistry, 1960. **64**: p. 519-24.
42. Feng, X. and L. Jiang, *Design and creation of superwetting/antiwetting surfaces.* Adv. Mater. (Weinheim, Ger.), 2006. **18**(23): p. 3063-3078.
43. Youngblood, J.P. and T.J. McCarthy, *Ultrahydrophobic Polymer Surfaces Prepared by Simultaneous Ablation of Polypropylene and Sputtering of Poly(tetrafluoroethylene) Using Radio Frequency Plasma.* Macromolecules, 1999. **32**(20): p. 6800-6806.
44. Dong, H., et al., *Superhydrophilic Surfaces via Polymer-SiO2 Nanocomposites.* Langmuir, 2010. **26**(19): p. 15567-15573.
45. Wu, Z., et al., *Antireflective and highly reflective coatings with self-cleaning properties from polymer and nanoparticle multilayers.* PMSE Prepr., 2006. **94**: p. 268-269.
46. Howarter, J.A. and J.P. Youngblood, *Self-cleaning and anti-fog surfaces via stimuli-responsive polymer brushes.* Adv. Mater. (Weinheim, Ger.), 2007. **19**(22): p. 3838-3843.
47. Huang, W. and H. Huang, *Progress in research on superhydrophilic coating.* Guangdong Huagong, 2008. **35**(10): p. 46-49.
48. Watanabe, H., et al., *Control of super hydrophobic and super hydrophilic surfaces of carbon nanowalls using atmospheric pressure plasma treatments.* Jpn. J. Appl. Phys., 2012. **51**(1, Pt. 2): p. 01AJ07/1-01AJ07/4.
49. Houmard, M., et al., *Enhanced cleanability of super-hydrophilic TiO2-SiO2 composite surfaces prepared via a sol-gel route.* Surf. Sci., 2011. **605**(3-4): p. 456-462.
50. Bravo, J., et al., *Transparent Superhydrophobic Films Based on Silica Nanoparticles.* Langmuir, 2007. **23**(13): p. 7293-7298.
51. Barthlott, W. and C. Neinhuis, *Purity of the sacred lotus, or escape from contamination in biological surfaces.* Planta, 1997. **202**(1): p. 1-8.

Vita

Guy Christopher Laine was born in Petersburg, Virginia. He was raised in Chester, VA where he graduated from Meadowbrook High School in 2002. He received his B.S degree in Chemical Engineering from Virginia Commonwealth University in 2006.